Engineering Analysis with Boundary Elements 103 (2019) 172–195

Contents lists available at ScienceDirect

Engineering Analysis with Boundary Elements

journal homepage: www.elsevier.com/locate/enganabound

Multiresolution-based adaptive central high resolution schemes for modeling of nonlinear propagating fronts

Hassan Yousefi [c,d], Timon Rabczuk [a,b,*]

[a] Division of Computational Mechanics, Ton Duc Thang University, Ho Chi Minh City, Viet Nam
[b] Faculty of Civil Engineering, Ton Duc Thang University, Ho Chi Minh City, Viet Nam
[c] Institute of Structural Mechanics (ISM), Bauhaus-University Weimar, Weimar 1599423, Germany
[d] School of Civil Engineering, Faculty of Engineering, University of Tehran, Tehran, Iran

ARTICLE INFO

MSC:
00-01
99-00

Keywords:
Interpolating wavelet
Adapted grid
Central high-resolution schemes
Second order accuracy
Nonlinear waves
Discontinuous fronts

ABSTRACT

A class of wavelet-based methods, which combine adaptive grids together with second-order central and central-upwind high-resolution schemes, is introduced for accurate solution of first order hyperbolic systems of conservation laws and related equations. It is shown that the proposed class recovers stability which otherwise may be lost when the underlying central schemes are utilized over non-uniform grids. For simulations on irregular grids, both full-discretized and semi-discretized forms are derived; in particular, the effect of using certain shifts of the center of the computational allow to use standard slope limiters on non-uniform cells. Thereafter, the questions of numerical entropy production, local truncation errors, and the Total Variation Diminishing (TVD) criterion for scalar equations, are investigated. Central schemes are sensitives for irregular grids. To cure this drawback in the present context of multiresolution, the adapted grid is locally modified around high-gradient zones by adding new neighboring points. For an adapted point of resolution scale j, the new points are locally added in both resolution j and all successive coarser resolutions. It is shown that this simple grid modification improves stability of numerical solutions; this, however, comes at the expense that cell-centered central and central-upwind high resolution schemes, may not satisfy the TVD property. Finally, we present numerical simulations for both scalar and systems of non-linear conservation laws which confirm the simplicity and efficiency of the proposed method. These simulations demonstrate the high accuracy, the entropy production of wavelet-based algorithms which can effectively detect high gradient zones of shock waves, rarefaction regions, and contact discontinuities.

1. Introduction

Multiresolution-based studying has rapidly been developed in many branches of science; one of such powerful schemes is the wavelet theory. Wavelets act as a mathematical microscope and can detect abrupt variations. Development of this theory is simultaneously done by scientists, mathematicians and engineers [1]. Wavelets can detect different local features of data separated locally in different resolutions. Wavelets can efficiently distinguish overall smooth variation of a solution from locally high transient ones. This multiresolution feature has interested many researchers in the field of partial differential equations (PDEs) [1]. One approach is to study problems in accordance with their solution variations; i.e., using different accuracy in different computational domains. In this approach, more grid points are concentrated around high-gradient zones to detect high variations. Such simulations lead to adaptive solvers. In this case, only the important physics of problems are precisely studied for a cost-effective computations. In general, wavelet-based adaptive methods have successfully been implemented for PDE solutions containing steep moving fronts or sharp transitions in small zones [2–9]. In the most of these approaches, wavelets are used as a tool to detect localized spatial behaviors and corresponding zones, also see [10–12]. Wavelet coefficients with considerable values concentrate automatically in the vicinity of high-gradient regions. The wavelet coefficients have a one to one correspondence with corresponding spatial grid points. Hence, by ignoring coefficients of small values and corresponding grid points, a considered grid can be adapted. In these grid-based adaptive schemes, the degrees of freedom are considered as point values in the physical space [13–15].

In this work, the propagation of nonlinear fronts are simulated by central high resolution schemes with proper integration of them with wavelet-based adaptation procedures. The accuracy and the effectiveness of numerical solutions can be obtained by such incorporation. In

* Corresponding author at: Division of Computational Mechanics, Ton Duc Thang University, Ho Chi Minh City, Viet Nam.
E-mail address: timon.rabczuk@tdtu.edu.vn (T. Rabczuk).

https://doi.org/10.1016/j.enganabound.2019.03.002
Received 19 October 2018; Received in revised form 9 February 2019; Accepted 6 March 2019
Available online 25 March 2019

numerical simulation of first order hyperbolic systems, several important and challenging features exist, as: the lack of inherent (natural) dissipation [16], the forming of artificial (numerical) dissipation and dispersion [17,18]. Inherent dissipation in a system improves both adaptation procedure and numerical stability. The numerical dispersion leads to developing wiggles in the front and behind of propagating waves, due to the distortion of different phases of propagating waves (fronts). The numerical dissipation has a tendency to flat discontinuities in numerical solutions [17,18]. Discontinuous solutions are commonly formed in non-linear first-order hyperbolic systems, where controlling both the numerical dissipation and dispersion are challenging. Despite of hyperbolic systems, the inherent dissipation exists in elliptic and parabolic PDEs [19]. These systems are not so sensitive to small perturbations in their numerical solutions. The perturbations or errors dissipate during numerical simulations. Based on this feature, wavelet-based adaptive schemes have successfully been employed in the modeling of the elliptic [20,21], parabolic problems [15,22,23] and parabolic-hyperbolic systems [24].

Considering hyperbolic problems, however, handling the artificial effects -dissipation and dispersion, needs special treatment. Significant non-physical oscillations would strongly form around the (nearly) discontinuous solutions: the Gibb's phenomenon. Due to such oscillations, numerical instability could occur. These spurious oscillations could propagate throughout the computational domain. Therefore, both the proper adaptation procedure and the stability of numerical solutions can fail.

To guarantee solution stability of high-resolution schemes on non-uniform grids, some conditions must be satisfied. Such assurance can be obtained by using the normalized variable and space formulation (NVSF) criterion [25]. This condition is successfully incorporated with wavelet-based adaptive methods for simulation of hyperbolic systems [10,26]. In the NVSF criterion, the identifying of propagating directions is necessary. This identification needs itself complex procedures, especially for 2-D and 3-D problems [26]. To remedy this disadvantage, in this work, central and central-upwind high resolution schemes are considered (like the Kurganov and Tadmor method) [27–29]. Central/central-upwind high resolution schemes on non-staggered grids offer the following benefits: having a simple and straightforward concept; being easy to implement; having less numerical dissipation than ones on the staggered cells, like the Nessyahu and Tadmor (NT) method; offering both semi-discrete and fully-discrete forms; being a Riemann-free solver; no requiring to staggered grid points as needed in the NT scheme [30]; having comparable second and higher order accuracy with other expensive techniques. Central/central-upwind methods, however, are sensitive for cell irregularity; our investigations show that numerical instabilities appear rapidly in adaptive solutions. This is because, these methods do not originally satisfy the NVSF condition. To guarantee the numerical stability, two features should be studied: 1) the performance of slope/flux limiters on non-uniform grids; 2) the effects of grid density variation on numerical solutions and adaptation procedures. Most of slope limiters have been developed for working properly on uniform grids. Using of such limiters on irregular grids leads to unstable solutions. Abrupt changing of grid densities can also lead to instability, due to ill-posedness feature of irregular sampled data. To prevent this kind of instability, density variation of adapted grids should be checked. For achieving this purpose, adapted grids are locally modified in the vicinity of high-gradient zones to achieve local semi-uniform grid points (then an ill-posed problem is nearly replaced with a well-posed one). This modification is done in context of the multiresolution analysis by a post-processing stage. Considering an adapted grid, for each point of level resolution j_0, some extra new neighbor points are locally added. The new points are inserted in both the same resolution level (j_0) and all successive coarser resolution levels, i.e.: $j \in \{j_0 - 1, j_0 - 2, \ldots, J_{min}\}$. It will be shown that even-though grid modification improves numerical stability, there is no guarantee to have long-term stability. This is due to performance of slope/flux limiters on non-uniform cells. For non-uniform cells, one approach is to re-design limiters [31,32]. In this study, it will be shown how to use limiters without their definition modification. This will be done by re-locating cell centers only in some cells acting as transmitting cells. Investigations show that the proposed method leads to stable results comparable with those of NVSF-based schemes.

In nonlinear conservation laws, discontinuous solutions develop typically. Thereby, common error estimation concepts, mainly based on the Taylor expansion, can not be used. For this reason, the concept of the local truncation error is used to assess the convergence of solutions to weak ones as a practical approach [33,34]. Related formulations for such error estimation would be provided for 1-D and 2-D non-uniform cells. This kind of error has direct relationship with the Lip'-norm theory introduced by Tadmor et al. [35,36] for nonlinear 1-D scalar conservation laws with convex flux. The numerical results confirm that the local truncation error can also be used for the convergence study of 1-D systems or 2-D conservation laws, even with non-convex fluxes.

The uniqueness of numerical solutions is checked by the concept of numerical entropy production. Theoretically, the numerical entropy production is zero in smooth regions while less than zero around shocks and discontinuities [37,38]. This helps to study the quality of numerical results especially for ones without exact solutions. All calculations will directly be done on non-uniform grids.

Concepts of the local truncation error and numerical entropy production have been used for both grid and method adaptation [39–41]. Different concepts could lead to different adapted results, especially, some concepts may not capture some phenomena. Hence, proper choosing of a adaptation approach would be crucial. In this study, wavelets are used for grid/method adaptation. Adaptation performance of this theory would be compared with the above-mentioned two concepts.

Hyperbolic systems with non-convex fluxes would also be studied. These systems can explain important phenomena, such as: Euler equations of gas dynamic with a non-convex flux, polymer system used for the simulation of polymer flooding processes in enhanced oil recovery and mechanical wave equations with non-convex fluxes. It will be shown that even though numerical solutions converge to weak form solutions (controlled by the local truncation error), they may not be physical (real) ones due to the existence of complex waves in these problems [39]. In this work, wavelets are used to both grid and method adaptations for capturing properly physical solutions.

The Dubuc–Deslauriers (D-D) interpolating wavelets [13,14,42] are used for grid adaptation. This family has simple and straightforward algorithms with physical meaning. All calculations can then be done in the physical domain. The D-D wavelets use minimal spatial support for data reconstruction (approximation), and this is important, since: larger inter-distance in two sampled data is, smaller correlation between them exists [13–15].

Semi-discretized PDEs in spatial domain are solved in time by an explicit TVD integration method, such as the second order TVD Runge–Kutta scheme. As all spatio-temporal calculations are done in the physical domain, the method is simple and conceptually straightforward [15].

Finally it should be mentioned that different approaches were developed for handling discontinuous solutions, such as high resolution schemes [43–45], non-polynomial-based high resolution schemes [46], discontinuous Galerkin methods [44,47], meshfree collocation methods [48–51], the integration of finite elements with slope limiters [52,53].

This paper is composed of nine parts. Section 2: explaining the main concept of multiresolution-based grid adaptation by interpolating wavelets; Section 3: presenting post-processing of adapted girds; Section 4: explaining the main concept of central or central-upwind scheme with cell-centered cell points; Section 5: estimation of the numerical entropy production; Section 6: evaluating of local truncation errors on 1-D and 2-D non-uniform grids; Section 7: explanation of the TVD conditions on non-uniform grids; Section 8: representing some 1-D and 2-D numerical examples. The conclusion is presented at the end of the paper.

2. Multiresolution analysis and adaptation of 1-D grids

2.1. Multiresolution representation of 1-D grids

A dyadic grid on spatial interval [0, 1] is assumed as follows [14]:

$$V_j = \left\{ x_{j,k} \in [0,1] : \; x_{j,k} = \frac{k}{2^j} \quad \text{for all} \quad j \in \mathbb{Z}, \text{and } k \in \{0,1,\dots,2^j\} \right\}, \tag{2.1}$$

where j and k are the resolution level (corresponding to spatial scale $1/2^j$) and spatial position ($k/2^j$), respectively. This definition of dyadic grid points V_j in Eq. (2.1) leads to the condition $x_{j-1,k} = x_{j,2k}$ and the multiresolution representation core: i.e., $V_j \subset V_{j+1}$. The points belongs to $V_{j+1} \setminus V_j$ is denoted by W_j, and it can be expressed as:

$$W_j = \left\{ \{ x_{j+1,2k+1} \in (0,1) : \; x_{j+1,2k+1} = \frac{2k+1}{2^{j+1}} \right.$$
$$\left. \text{for all} \quad j \in \mathbb{Z}, \text{ and } k \in \{0,1,\dots,2^j - 1\} \right\}.$$

So it can intuitively be concluded that: $V_j \oplus W_j = V_{j+1}$. This means the detail subspace W_j with the approximation subspace V_j can create (span) the next finer approximation subspace V_{j+1} with more details. By repeating this decomposition procedure on $V_{J_{max}}$, it is obvious that:

$$V_{J_{\max}} = V_{J_{\min}} \oplus \sum_{i=0}^{N_d} W_{J_{\min}+i}, \qquad N_d = J_{\max} - J_{\min} - 1,$$

where, J_{max}, J_{min} and N_d denote the finest resolution, the coarsest resolution and number of decomposing levels, respectively [42].

A continuous function $f(x)$, defined on $V_{J_{max}}$, is assumed (i.e., $x \in V_{J_{max}}$). Regarding the multiresolution representation, the function can be decomposed as [14,42]:

$$f(x) = \sum_{l=0}^{2^{J_{\min}}} c_{J_{\min},l} \phi_{J_{\min},l}(x) + \sum_{j=J_{\min}}^{J_{\max}-1} \sum_{n=0}^{2^j-1} d_{j,n} \psi_{j,n}(x)$$
$$= \mathrm{P} f_{J_{min}} + \sum_{j=J_{min}}^{J_{max}-1} \mathrm{Q} f_j,$$

where $\phi(x)$ and $\psi(x)$ are scaling and wavelet functions, respectively; sets $\{\phi_{j,k}\}$ and $\{\psi_{j,l}\}$ denote dilated and shifted versions of $\phi(x)$ and $\psi(x)$, respectively. Coefficients $c_{j,l}$ and $d_{j,k}$ are respectively approximation and detail coefficients with resolution j. The operators $\mathrm{P}f_j$ and $\mathrm{Q}f_j$ show the approximation and detail information of $f(x)$, defined on grid points V_j, and W_j, respectively. The approximation on successive finer resolution $j+1$, can then be obtained as: $\mathrm{P}f_{j+1} = \mathrm{P}f_j + \mathrm{Q}f_j$ [42].

In this study, the interpolating D-D wavelet of order $2M-1$ with support $\mathrm{Supp}(\phi) = [-2M+1, 2M-1]$ is used. It can be obtained by auto-correlation of the Daubechies scaling function of order M (having M vanishing moments) [42]. By using this family, the transform coefficients in Eq. (2.2) can totally be evaluated in the physical space with physical meanings. The approximation coefficients ($c_{J_{min},l}$) are equal to sampled values of $f(x)$ at points $x_{J_{min},l} \in V_{J_{min}}$, and the detail coefficients ($d_{j,n}$) are differences between $f(x_{j+1,2n+1})$ and $\mathrm{P}f_{j+1}(x_{j+1,2n+1})$, or $d_{j,n} = f(x_{j+1,2n+1}) - \mathrm{P}f_{j+1}(x_{j+1,2n+1})$ (for the D-D wavelets, $\mathrm{P}f_{j+1}(x_{j+1,2n+1})$ can be obtained by the local Lagrange interpolation on points V_j); for details see [13,14,42].

In the interpolating wavelet theory, transform coefficients and grid points have one-to-one correspondence. This feature leads to a simple 1-D grid adaptation algorithm. For $f(x) \in V_{J_{max}}$, a predefined threshold ϵ is assumed, then, in each level of resolution $j \in \{J_{min}, J_{min}+1, \dots, J_{max}-1\}$, points $x_{j+1,2n+1} \in W_j$ are omitted from original calculating grid points, if corresponding detail coefficients, $d_{j,n}$ satisfy the condition $d_{j,n} < \epsilon$. This means that the function at the point $x_{j+1,2n+1}$ is smooth enough, so that its contribution in the approximation, $d_{j,n}\psi_{j,n}(x)$, can be neglected (see Eq. (2.2)). Donoho [54] showed that such truncation error is in accordance with threshold values. Finally it should be mentioned that the predefined threshold can be either level-dependent or not. One popular level-dependent threshold is $\epsilon_j = \epsilon_0 / 2^{J_{max}-j-1}$ for $j \in \{J_{min}, J_{min}+1, \dots J_{max}-1\}$. This means a smaller threshold is assumed for finer resolution. To use a constant threshold value for all resolution levels, it is better to normalize the detail coefficient of resolution j as: $d_{j,n} = d_{j,n} / f_j^{ref}$. In this study constant pre-defined threshold with normalized factor $f_j^{ref} = \max\{f(x_j)\}$ is used.

The presented adaptation procedure was shown to be efficient in the resolution of scalar functions. For resolution of functions in vector system, the previous procedure is modified to reflect the solutions' behaviors of all equations. Namely, the resultant adapted grid is simply superposition of all adapted grids; which each adapted grid corresponds to a functions of the vector system.

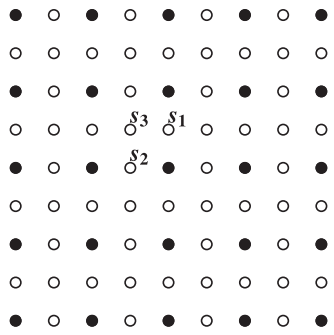

Fig. 1. Spatial locations of points belonging to subspaces V_2 and V_3, where $\bullet \in V_2$ and $\bullet \cup \circ \in V_3$, for $(x_i, y_j) \in [0,1] \times [0,1]$.

2.2. Multiresolution representation of 2-D grids

Consider a uniform grid of spatial locations $(x, y) \in [0,1] \times [0,1]$; a set of points belonging to subspace V_j can be defined as [26]:

$$V_j = \left\{ \{ (x_{j,k}, y_{j,l}) : \; x_{j,k} = k2^{-j}, \; y_{j,l} = l2^{-j} \right\} \quad \text{for all} \quad j,k,l \in \mathbb{Z}, \tag{2.2}$$

where j denotes resolution level and $J_{min} \le j \le J_{max}$; coefficients k & l measure spatial locations. Fig. 1 illustrates a schematic representation of points belonging to V_j ($\bullet \in V_j$) and V_{j+1} ($\bullet \cup \circ \in V_{j+1}$) for case $j = 2$.

Same as the 1-D case, for 2-D information a detail subspace W_j belonging to subspace $V_{j+1} \setminus V_j$ can be defined. These points are shown in Fig. 1 with hollow circles; i.e.: $\circ \in W_j$. In this detail sub-space, three point types s_1, s_2 and s_3 can be distinguished, as:

1. Points in even-numbered points in the x direction and odd-numbered in the y direction; i.e., set $s_1 = \{(x_{j+1,2k}, y_{j+1,2l+1})\}$,
2. Points in odd-numbered points in the x direction and even-numbered in the y direction; i.e., set $s_2 = \{(x_{j+1,2k+1}, y_{j+1,2l})\}$,
3. Odd-numbered grid points in both directions: $s_3 = \{(x_{j+1,2k+1}, y_{j+1,2l+1})\}$.

Based on the subspaces V_j and W_j, a 2-D multiresolution analysis can be obtained as the 1-D case. For point sets $\{(x_{j,k}, y_{j,l}) \in s_i : i \in \{1,2,3\}\}$, four wavelet coefficients $\left\{ d^i_{j,\{k,l\}} : \; i \in \{1,2,3,4\} \right\}$ can be defined as:

1. For points s_1, wavelet coefficients are $d^1_{j,\{k,l\}}$; they measure local variations in vertical (y) direction,
2. For points s_2, wavelet coefficients are $d^2_{j,\{k,l\}}$; they measure local variations in horizontal (x) direction,
3. For points s_3, two sets of wavelet coefficients can be defined as $d^3_{j,\{k,l\}}$ and $d^4_{j,\{k,l\}}$; they measure respectively local variations in x and y directions.

These coefficients can be evaluated by the 1-D wavelet transform algorithm [26]. For 2-D grid adaptation, by considering a threshold value, grid points can then be adapted as the $1-D$ case [26].

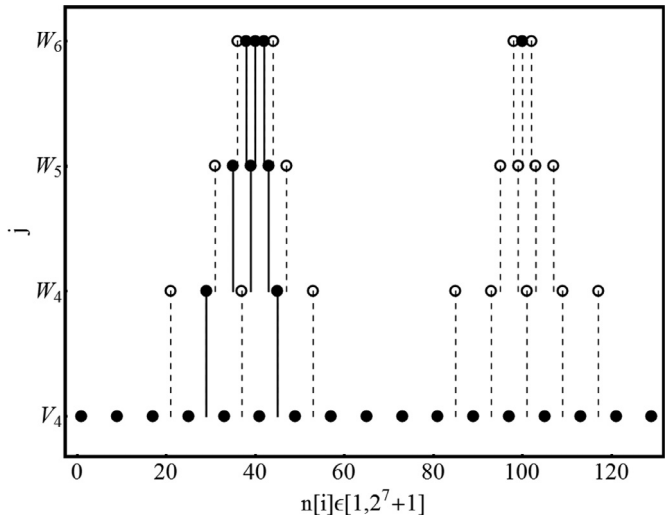

Fig. 2. Modification of an adapted grid; solid points and hollow circles correspond to adapted and extra added points, respectively. For grid modification stage, we assume: $N_s = N_c = 1$.

3. Post processing the adapted grid points

Once adapted grids are obtained via the aforementioned wavelet-based procedures, grids are modified considering resolution level of each point; this is done to guarantee gradual density variation of grid points.

3.1. 1-D grid modification

The procedure for modification of 1-D adapted grids can be summarized as:

1. Setting the level resolution (j) equal to the finest resolution, i.e.: $j = J_{max} - 1$,
2. Considering points belonging to the detail space of resolution j; i.e., points: $\{x_{j+1,2k+1} = (2k+1)/2^{j+1} \in W_j\}$,
3. Existence controlling of N_s neighbor-points for each side of the point $x_{j,k} \in W_j$ at the same level of resolution, i.e., points: $\{x_{j+1,2(k+i)+1} : \quad i \in \{-N_s, -N_s+1, \dots, N_s\}, \quad i \neq 0\}$,
4. Existence controlling of N_c neighbor-points for each side of the point $x_{j,k} \in W_j$ at the successive coarser resolution (subspace W_{j-1}). This step is only done for levels $j > J_{min}$,
5. Adding the extra points from steps 3 and 4 to the adapted grid (updating the modified adapted grid),
6. If $j > J_{min}$, set $j = j - 1$ and then following steps 2 through 6,
7. If $j = J_{min}$, consider only steps 2 and 3. These points are added to the updated adapted grid points, as the final stage.

The already-mentioned post processing procedure is illustrated in Fig. 2; there, distribution of adapted grid points is shown in different levels of resolution. Solid points correspond to assumed (original) adapted points and the hollow ones associate with points obtained after the post-processing procedure. This modification leads to locally semi-uniform distributions.

3.2. 2-D grid modification

The 2-D grid modification will be done by controlling and adding new points in the same and coarser resolution levels, as the 1-D grid case. For this purpose, for different points s_1, s_2 or s_3 (Fig. 1), different adding procedures will be considered.

3.2.1. Adding extra new points by the multiresolution concept

Adding in the same resolution. Depending on point type (s_1, s_2 or s_3), different inserting procedures will be considered; different neighbor points will be added for each point s_1, s_2 or s_3, see Fig. 3. There, for an adapted point belonging to W_2, new neighbor points of W_2 are locally added. In this figure, bright gray solid points are the new extra points added around each point s_1, s_2 or s_3. In this figure, only one row or column of the nearest points is considered for modification stage. In general, more surrounding points of W_2 can be considered for each point s_1, s_2 or s_3.

Adding in the successive coarser resolution. In this case, for a point belonging to W_j some new surrounding points including in W_{j-1} are added. To guarantee symmetry and gradual concentration of modified adapted points, it may also be necessary to consider some extra points from sub-space V_{j-1}. For different points s_1, s_2 and s_3, different neighbor points will be considered. Such grid checking/adding procedures are shown in Fig. 4. In each illustration, points denoted by w belong to sub-space $W_{j-1} = W_{2-1}$ and points with name v belongs to the sub-space $V_{j-1} = V_{2-1}$. In these figures, only one row or column of the nearest distance is considered.

3.3. Post-processing 2-D adapted grids

The modification algorithm for 2-D grids is generally similar to the 1-D case; it can be reviewed as follows:

1. Set the level resolution j (where $J_{min} \le j \le J_{max} - 1$) equal to the finest resolution level; i.e., $j = J_{max} - 1$ (with spatial sampling steps $dx = dy = 1/2^{J_{max}-1}$),
2. Consider the set of points corresponding to detail sub-space of resolution j; i.e., points $\{(x_{j,k}, y_{j,l}) \in W_j\}$,
3. Control N_s neighbor-rows or columns of surrounding points for each side of the point $(x_{j,k}, y_{j,l})$; this control is done at the same level of resolution,
4. Control N_c neighbor-rows or columns of points for each side of the point $(x_{j,k}, y_{j,l})$; this is done at the successive coarser resolution (subspace W_{j-1}),
5. Regarding step 3, add the surrounding points in subspace W_j,

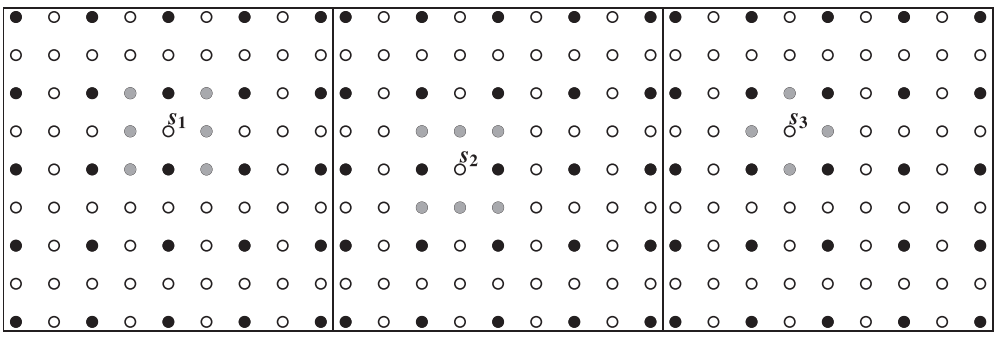

Fig. 3. Adding procedure in the same resolution for point types s_1, s_2 or s_3, where $\bullet \in V_2$, $\bullet \cup \circ \in V_3$, $\circ \in W_2$ and bright gray solid points are the added points belonging to W_2.

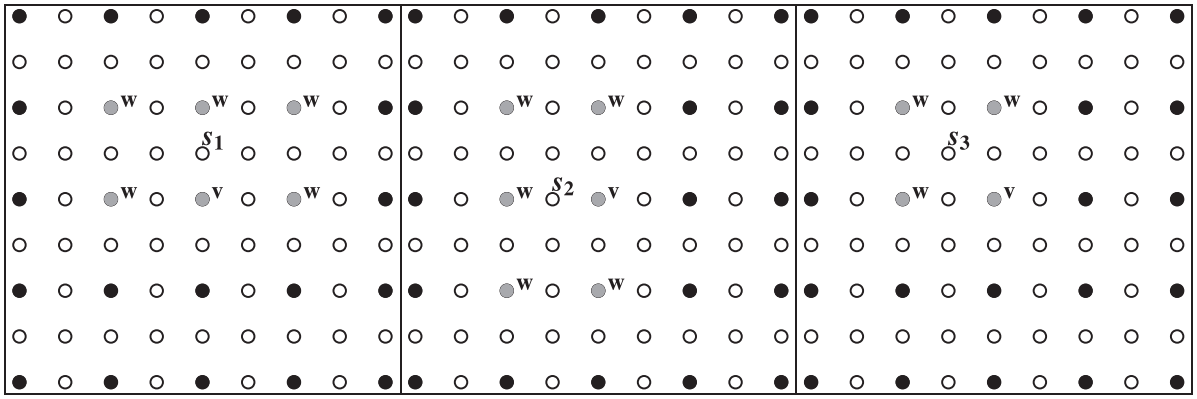

Fig. 4. Adding procedure in the successive coarser resolution for point types s_1, s_2 or s_3, where $\bullet \in V_2$, $\bullet \cup \circ \in V_3$, $\circ \in W_2$ and bright gray solid points are the added points belonging to V_2.

6. Considering step 4, add the surrounding points in subspace W_{j-1}; in this stage, it may also be needed to add some new points in the sub-space V_{j-1} (as explained before),
7. If $j > J_{min}$, set $j = j - 1$ and go back to step 2, else go to step 8,
8. If $j = J_{min}$, consider only steps 2, 3 and 5.

4. Central and upwind-central high resolution schemes of spatially second order accuracy

4.1. One-dimensional formulations

Here, the semi-discretized form of a scalar first-order hyperbolic system, $u_t + F(u)_x = 0$, will be provided for the KT method [27] and two other improvements of this scheme (to have less numerical dissipation) [28,29]. By following the concept of the Reconstruction/Evolution/Projection (REP) procedure [27] for cell-centered non-uniform cells, it is easy to show that for jth cell, the semi-discrete form is:

$$\frac{du_j}{dt} + \frac{F^*_{j+1/2} - F^*_{j-1/2}}{\Delta x_j} = 0, \qquad F^*_{j\pm 1/2} := F\left(u^*_{j\pm 1/2}\right), \tag{4.1}$$

where u_j denotes cell center solution (estimated state values) on jth cell; $\Delta x_j := x_{j+1/2} - x_{j-1/2}$ is the jth cell length; and $F(u^*_{j\pm 1/2})$ shows a proper combination of left and right reconstructed state values and corresponding fluxes at cell edges $x_{j\pm 1/2}$. The left and right reconstructed state values are shown respectively by $u^L_{j+1/2}$ and $u^R_{j+1/2}$. These values can be evaluated as $u^L_{j+1/2} := u_i + (u_x)_j (x_{j+1/2} - x_j)$ and $u^R_{j+1/2} := u_{j+1} - (u_x)_{j+1}(x_{j+1} - x_{j+1/2})$ for spatially second order methods, where $(u_x)_j$ denotes a limited slope at point x_j.

The two improvements of the central KT scheme are central-upwind methods, noting here by $M1$ and $M2$. They use two different maximum local propagation speeds for right and left directions at cell edges $x_{j+1/2}$. The speeds are shown by $a^R_{j+1/2}$ and $a^L_{j+1/2}$ for right and left directions, respectively. Such speed distinguishing leads to a narrower non-smooth zone around cell edge $x_{j+1/2}$, and therefore less dissipative schemes. The scheme $M2$ is an improvement of the $M1$ method using a narrower non-smooth zone; for more details see [28,29].

Expressed in terms of the left and right states $F^{L/R}_{i+1/2} := F(u^{L/R}_{i+1/2})$, the reconstructed fluxes for the KT, $M1$ and $M2$ schemes are:

1. The central KT scheme:

$$F^*_{i+1/2} := \frac{1}{2}\left[F^R_{i+1/2} + F^L_{i+1/2}\right] - \frac{1}{2}a_{i+1/2}\left[u^R_{i+1/2} - u^L_{i+1/2}\right]. \tag{4.2}$$

2. For the central-upwind method $M1$:

$$F^*_{i+1/2} := \frac{a^R_{i+1/2}F^L_{i+1/2} - a^L_{i+1/2}F^R_{i+1/2}}{a^R_{i+1/2} - a^L_{i+1/2}} + a^L_{i+1/2}a^R_{i+1/2}\frac{u^R_{i+1/2} - u^L_{i+1/2}}{a^R_{i+1/2} - a^L_{i+1/2}}. \tag{4.3}$$

3. For the central-upwind method $M2$:

$$F^*_{i+1/2} := \frac{a^R_{i+1/2}F^L_{i+1/2} - a^L_{i+1/2}F^R_{i+1/2}}{a^R_{i+1/2} - a^L_{i+1/2}} + \frac{a^L_{i+1/2}a^R_{i+1/2}}{2} \times \frac{u^R_{i+1/2} - u^L_{i+1/2}}{a^R_{i+1/2} - a^L_{i+1/2}}. \tag{4.4}$$

For non-centered non-uniform cells, it can be shown (see Appendix A) that in the sense of average solutions, the semi discrete form of central schemes is:

$$\frac{d\bar{u}_j}{dt} + \frac{F^*_{j+1/2} - F^*_{j-1/2}}{\Delta x_j} = 0, \qquad F^*_{j\pm 1/2} := F\left(u^*_{j\pm 1/2}\right), \tag{4.5}$$

where $\bar{u}_j$ denotes cell average solution.

Multidimensional problems are discretized based on the 1-D formulations in Eqs. (4.1)–(4.5) simply by the *dimension-by-dimension* approach [27].

5. Numerical entropy production of central/central-upwind schemes

Calculation of numerical entropy production helps one to control quality/uniqueness of numerical results especially for ones without exact solutions. This is because, theoretically, the numerical entropy production is zero in smooth regions while less than zero around shocks and discontinuities.

Puppo [37,38] showed how to estimate the numerical entropy production for staggered central high resolution schemes. After these works, Puppo et al. [40] improved the previous works for non-staggered central/central-upwind schemes.

The entropy function $\eta(u)$ with flux $\psi(u)$ satisfies the relationship:

$$\eta_t + \psi_x(u) \le 0, \qquad \eta := \eta(x).$$

Following works [37,38], by integrating this relationship in spatio-temporal volume $[x_j - \frac{\Delta x_j}{2}, x_j + \frac{\Delta x_j}{2}] \times [t^n, t^{n+1}]$, and discretizing the inequality by considering the REP concept (used in the KT, $M1$ or $M2$ method), we have:

$$\eta^{n+1}_j - \left(\eta^n_j - \frac{1}{\Delta x_j}\int_{t^n}^{t^{n+1}} \left[\psi^*_{j+1/2} - \psi^*_{j-1/2}\right]\right) \le 0, \qquad \eta^n_j := \eta(x_j, t^n). \tag{5.1}$$

Based on this inequality, the density of numerical entropy production at x_j, S_j^n, can be defined as:

$$S_j^n = \frac{1}{\Delta x_j}\left\{\eta_j^{n+1} - \left(\eta_j^n - \frac{1}{\Delta x_j}\int_{t^n}^{t^{n+1}}\left[\psi_{j+1/2}^* - \psi_{j-1/2}^*\right]\right)\right\}, \quad S_j^n := S(x_j, t^n), \tag{5.2}$$

where $\psi_{j\pm1/2}^* := \psi_{j\pm1/2}^*((u_{j\pm1/2}^L)^n, (u_{j\pm1/2}^R)^n)$.

In Eqs. (5.1) and (5.2), the terms in parentheses estimate the evolved values of the entropy at the next time step (this can be done with the KT, $M1$ or $M2$ method). Theoretically, as mentioned before, the parameter S_j^n is zero in smooth regions, however, in numerical solutions, it may be slightly less or more than zero [40]. This kind of entropy definition cannot efficiently detect some phenomena like contact discontinuities even by increasing number of resolution levels (see the Sod and the Lax problems in the Euler gas dynamic system). To remedy this, other approaches like the entropy viscosity scheme can be recommended [55].

6. Local truncation error on non-uniform cells

6.1. One dimensional systems

The aim of this section is to estimate local truncation errors in hyperbolic systems of conservation laws with the governing equation: $u_t + (F(u))_x = 0,\ u(x, t = 0) = u_0(x)$.

It is easy to show that solution of this equation is also a weak solution satisfying the relationship:

$$E(u,\phi) = -\int_{t=0}^{\infty}\int_X \left\{u(x,t)\phi_t(x,t) + F(u(x,t))\phi_x(x,t)\right\}\mathrm{d}x\mathrm{d}t + \int_X \left\{u(x,t)\phi_t(x,t)\right\}\mathrm{d}x = 0, \tag{6.1}$$

where $\phi(x, t)$ is a test function that $\phi(x,t) \in C_0^\infty(X \times [0,\infty])$. One effective and practical way to measure convergence of a numerical solution $u(x, t)$ is to check how much it fails to satisfy (6.1); this can be measured by evaluating $E(u, \phi)$ [33,34]. For a convex scalar hyperbolic system ($\mathrm{d}F(u)/\mathrm{d}(u) > \alpha > 0$), the function $E(u, \phi)$ measures point-wisely real errors in weak Lip'-norm; this norm is developed by Tadmor to measure errors in simulation of the non-linear scalar conservation laws [35,36]. In nonlinear conservation laws, discontinuous solutions develop typically; in these cases standard methods of error estimation are not valid. Such approaches consider the Taylor expansion which is based on the smoothness assumption.

The final point is the relationship of this local truncation error with the weak Lip'-norm theory studied for convex scalar one dimensional hyperbolic systems. Numerical results confirm that it is also an effective tool for systems of one dimensional PDEs, 2-D problems, and even non-convex systems.

To be sure that $E(u, \phi)$ measures errors of $u(x, t)$, some constraints should be met by the test function $\phi(x, t)$: 1) the space spanned by the test functions should have a higher order accuracy, so that the order of error $E(u, \phi)$ is affected by solutions $u(x, t)$; 2) the test function have continuous derivatives; 3) to estimate locally the error $E(u, \phi)$, the test function has to be compact support in spatio-temporal domains.

We now consider the truncation error $E_j^n := E(u^\Delta, \phi)$ for the piecewise constant approximate solution $u^\Delta(x, t)$

$$u^\Delta(x,t) = \sum_{j,n} u_j^n \times \mathbf{1}_{C_j\times T^n}(x,t),$$
$$C_j \times T^n := \left[x_{j-1/2}, x_{j+1/2}\right] \times \left[t^{n-1/2}, t^{n+1/2}\right],$$

The compact test function $\phi(x, t)$ is assumed to be $\phi_j^n(x,t) := B_j(x)B^n(t)$, where $B_j(x)$ and $B^n(t)$ are the quadratic B-splines with center points $x = x_j$ and $t = t^n$. In this case, supports of $B_j(x)$ and $B^n(t)$ belong to $x \in [x_{j-3/2}, x_{j+3/2}]$ and $t \in [t^{n-3/2}, t^{n+3/2}]$, respectively.

To obtain higher-order B-splines, the *recurrence feature* between higher-order and lower-order B-splines: recall that the B-spline of order k with centered position j can be obtained as,

$$B_{j,k} = B_{j,k-1}w_{j,k} + B_{j+1,k}\left(1 - w_{j+1,k}\right),$$
$$w_{j,k}(x) := \begin{cases} \frac{x - x_j}{x_{j+k-1} - x_j}, & \text{if } x_j \neq x_{j+k-1}, \\ 0, & \text{otherwise.} \end{cases} \tag{6.2}$$

B-splines should also satisfy the partition of unity condition $\sum_j B_{j,k}(x) \equiv 1$.

Let us consider three successive cells, with length ratios, $a = \Delta x_{j-1}/\Delta x_j$ and $b = \Delta x_{j+1}/\Delta x_j$, where $\Delta x_j := x_{j+1/2} - x_{j-1/2}$ denotes jth cell length with cell middle point x_j. It is easy to show that $B_j(x)$ is:

$$B_j(x) = \begin{cases} \frac{(2x - 2x_j + \Delta x + 2a\Delta x)^2}{4a(1+a)\Delta x^2}, & \text{if } x_{j-3/2} \le x \le x_{j-1/2}, \\ \frac{-4(2+a+b)\left(x-x_j\right)^2 - 4(a-b)(x-x_j)\Delta x + (2+3b+a(3+4b))\Delta x^2}{4(1+a)(1+b)\Delta x^2}, & \text{if } x_{j-1/2} \le x \le x_{j+1/2}, \\ \frac{(-2x + 2x_j + \Delta x + 2b\Delta x)^2}{4b(1+b)\Delta x^2}, & \text{if } x_{j+1/2} \le x \le x_{j+3/2}, \\ 0, & \text{otherwise,} \end{cases} \tag{6.3}$$

where: $\Delta x := \Delta x_j$; $x_j = (x_{j-1/2} + x_{j+1/2})/2$; $x_{j-3/2} := x_j - \Delta x(1/2 + a)$; $x_{j-1/2} := x_j - \Delta x/2$; $x_{j+3/2} := x_j + \Delta x(1/2 + b)$; $x_{j+1/2} := x_j + \Delta x/2$.

It is easy to check that on uniform grids, where $a = b = 1$, the above-mentioned B-spline definition leads to the B-spline on uniform grids. Since in time-domain, in this study, a constant time-step is used, the definition of $B^n(t)$ is the quadratic B-spline on uniform grids with step Δt, as:

$$B^n(x) = \begin{cases} \frac{\left(t - t^{n-3/2}\right)^2}{2\Delta t^2}, & \text{if } t^{n-\frac{3}{2}} \le t \le t^{n-\frac{1}{2}}, \\ \frac{3}{4} - \frac{(t-t^n)^2}{\Delta t^2}, & \text{if } t^{n-\frac{1}{2}} \le t \le t^{n+\frac{1}{2}}, \\ \frac{\left(t - t^{n+3/2}\right)^2}{2\Delta t^2}, & \text{if } t^{n+\frac{1}{2}} \le t \le t^{n+\frac{3}{2}}, \\ 0, & \text{otherwise,} \end{cases} \tag{6.4}$$

here: $t^{n\pm\frac{1}{2}} := (t_n \pm \frac{\Delta t}{2})$ and $t^{n\pm\frac{3}{2}} := (t_n \pm \frac{3}{2}\Delta t)$.

For spatially non-uniform grid points, it is straightforward to show that the local truncation error can be expressed as:

$$E_j^n = \Delta x \mathcal{U}_j^n + \Delta t \mathcal{F}_j^n, \tag{6.5}$$

where $\mathcal{U}_j^n$ is expressed in terms of the time differences $\Delta u_\alpha^n := 1/2\left(u_\alpha^{n+1} - u_\alpha^{n-1}\right)$,

$$\mathcal{U}_j^n = \frac{a^2}{3(a+1)}\Delta u_{j-1}^n + \frac{(a(3b+2)+2b+1)}{3(a+1)(b+1)}\Delta u_j^n + \frac{b^2}{3(b+1)}\Delta u_{j+1}^n,$$

and $\mathcal{F}_j^n$ is expressed in terms of the time averages $\mu F_\alpha^n := 1/6\left(F_\alpha^{n-1} + 4F_\alpha^n + F_\alpha^{n+1}\right)$,

$$\mathcal{F}_j^n = -\frac{(b-a)}{(a+1)(b+1)}\mu F_j^n - \frac{a}{a+1}\mu F_{j-1}^n + \frac{b}{b+1}\mu F_{j+1}^n.$$

6.2. Two-dimensional problems

Let us consider a two dimensional scalar hyperbolic PDE as:

$$u_t + F(u)_x + G(u)_y = 0, \qquad u_0(x,y) := u(x,y,t=0). \tag{6.6}$$

As in the 1-D case, the weak solution of (6.6) satisfies

$$E(u,\phi) = -\int_{t=0}^{\infty}\int_{\Omega} u(x,y,t)\phi_t(x,y,t) + F(u(x,y,t))\phi_x(x,y,t) + G(u(x,y,t))\phi_y(x,y,t)\,\mathrm{d}x\mathrm{d}y\mathrm{d}t + \int_{\Omega} u(x,y,t)\phi_t(x,y,t)\,\mathrm{d}x\mathrm{d}y = 0. \tag{6.7}$$

We quantify the truncation error $E^n_{j,k} := E(u^\Delta, \phi)$ for the piecewise constant approximate solution, $u^\Delta(x,y,t)$,

$$u^\Delta(x,y,t) := \sum_{j,k,n} u^n_{j,k} \times \mathbf{1}_{C_{j,k}\times T^n}(x,y,t) \quad C_{j,k}\times T^n := \left[x_{j-1/2}, x_{j+1/2}\right] \times \left[y_{k-1/2}, y_{k+1/2}\right] \times \left[t^{n-1/2}, t^{n+1/2}\right].$$

The test function $\phi(x, y, t)$ can also be defined as: $\phi^n_{j,k}(x,y,t) := B_j(x)B_k(y)B^n(t)$. Where all functions $B_j(x)$, $B_k(y)$ (from (6.3)), and $B^n(t)$ (from (6.4)) denote quadratic B-splines. Let us assume the successive cell length ratios in x and y directions to be: $\{a = \frac{\Delta x_{j-1}}{\Delta x_j},\ b = \frac{\Delta x_{j+1}}{\Delta x_j}\}$ and $\{c = \frac{\Delta y_{k-1}}{\Delta y_k},\ d = \frac{\Delta y_{k+1}}{\Delta y_k}\}$, where: $\Delta x = \Delta x_j := x_{j+1/2} - x_{j-1/2}$ and $\Delta y = \Delta y_k := y_{k+1/2} - y_{k-1/2}$. By these assumptions, the local truncation error $E^n_{j,k}$ can be represented as:

$$E^n_{j,k} = \left\{\Delta x\Delta y\mathcal{U}^n_{j,k} + \Delta t\Delta y\mathcal{F}^n_{j,k} + \Delta t\Delta x\mathcal{G}^n_{j,k}\right\}, \tag{6.8}$$

where $\mathcal{U}^n_{j,k}$ is expressed in terms of the time differences $\Delta u^n_{\alpha,\beta} := 1/2(u^{n+1}_{\alpha,\beta} - u^{n-1}_{\alpha,\beta})$

$$\begin{aligned}\mathcal{U}^n_{j,k} =\ & \frac{a^2d^3}{9(a+1)b(b+1)}\Delta u^n_{j-1,k+1} + \frac{a^2(a(3b+2)+2b+1)u^{n-1}_{j-1,k}}{9(a+1)^2(b+1)}\Delta u^n_{j-1,k} \\ & + \frac{b^2c^3}{9a(a+1)(b+1)}\Delta u^n_{j+1,k-1} + \frac{b^2(a(3b+2)+2b+1)}{9(a+1)(b+1)^2}\Delta u^n_{j+1,k} \\ & + \frac{c^3(a(3b+2)+2b+1)}{9a(a+1)^2(b+1)}\Delta u^n_{j,k-1} + \frac{d^3(a(3b+2)+2b+1)}{9(a+1)b(b+1)^2}\Delta u^n_{j,k+1} \\ & + \frac{(a(3b+2)+2b+1)^2}{9(a+1)^2(b+1)^2}\Delta u^n_{j,k} + \frac{ac^3}{9(a+1)^2}\Delta u^n_{j-1,k-1} \\ & + \frac{bd^3u^{n-1}_{j+1,k+1}}{9(b+1)^2}\Delta u^n_{j+1,k+1},\end{aligned}$$

and $\mathcal{F}^n_{j,k}$ and $\mathcal{G}^n_{j,k}$ are expressed in terms of the time averages $\mu Z^n_{\alpha,\beta} := 1/6(Z^{n-1}_{\alpha,\beta} + 4Z^n_{\alpha,\beta} + Z^{n+1}_{\alpha,\beta})$,

$$\begin{aligned}\mathcal{F}^n_{j,k} =\ & -\frac{c^3}{3(a+1)^2}\mu F^n_{j-1,k-1} + \frac{(a-b)c^3}{3a(a+1)^2(b+1)}\mu F^n_{j,k-1} \\ & + \frac{bc^3}{3\left(a^2+a\right)(b+1)}\mu F^n_{j+1,k-1} \\ & - \frac{a(2b+a(3b+2)+1)}{3(a+1)^2(b+1)}\mu F^n_{j-1,k} - \frac{ad^3}{3(a+1)\left(b^2+b\right)}\mu F^n \\ & + \frac{(a-b)(2b+a(3b+2)+1)}{3(a+1)^2(b+1)^2}\mu F^n_{j,k} \\ & \frac{(a-b)d^3}{3(a+1)b(b+1)^2}\mu F^n_{j,k+1} + \frac{b(2b+a(3b+2)+1)}{3(a+1)(b+1)^2}\mu F^n_{j+1,k} \\ & + \frac{d^3}{3(b+1)^2}\mu F^n_{j+1,k+1},\end{aligned}$$

$$\begin{aligned}\mathcal{G}^n_{j,k} =\ & -\frac{c^2b^2}{3\left(a^2+a\right)(b+1)}\mu G^n_{j+1,k-1} + \frac{(a-b)b^2}{3(a+1)(b+1)^2}\mu G^n_{j+1,k} \\ & + \frac{d^2b}{3(b+1)^2}\mu G^n_{j+1,k+1} \\ & - \frac{ac^2}{3(a+1)^2}\mu G^n_{j-1,k-1} + \frac{a^2(a-b)}{3(a+1)^2(b+1)}\mu G^n_{j-1,k} \\ & + \frac{a^2d^2}{3(a+1)\left(b^2+b\right)}\mu G^n_{j-1,k+1} \\ & - \frac{c^2(2b+a(3b+2)+1)}{3a(a+1)^2(b+1)}\mu G^n_{j,k-1} + \frac{(a-b)(2b+a(3b+2)+1)}{3(a+1)^2(b+1)^2}\mu G^n_{j,k} \\ & + \frac{d^2(2b+a(3b+2)+1)}{3(a+1)(b+1)^2b}\mu G^n_{j,k+1}.\end{aligned}$$

7. The TVD property of semi-discrete schemes

7.1. Global and local TVD conditions

To control the development of spurious oscillations in numerical simulation of hyperbolic systems, it is necessary to show that a monotone (non-increasing or non-decreasing) profile remains monotone during time evolution. To achieve high-order of accuracy, a relaxed monotonicity condition — so called Total Variation Diminishing (TVD) is sought [43,56]. We consider a general class of non-linear semi-discrete scalar scheme which takes the *incremental form*

$$\frac{du_i}{dt} = C^+_{i+1/2}(u_{i+1} - u_i) - C^-_{i-1/2}(u_i - u_{i-1}), \qquad u_i := u_i(t).$$

A general (global) TVD condition derived in [56] is expressed in terms of the global positivity condition, e.g.,[57–59]:

$$C^+_{i+1/2} \geq 0,\ C^-_{i+1/2} \geq 0,\ C^+_{i+1/2} + C^-_{i+1/2} \leq 1. \tag{7.1}$$

Local TVD conditions were studied in [60] where it was shown that for the TVD property to hold, it suffice to verify the positivity condition (7.1) in the extreme cells and their surrounding grid points. In the present context of (4.1), these *local* TVD conditions amount to:

1. In extreme points, for both uniform and non-uniform cells, the numerical fluxes $F^*_{i\pm1/2}$ satisfy (see [60], Lemma 2.1):
   (a) at maximum values u_i : $F^*_{i+1/2} \geq F^*_{i-1/2}$,
   (b) at minimum values u_i : $F^*_{i+1/2} \leq F^*_{i-1/2}$,
2. Oshor [61] showed that in order to satisfy the positivity conditions, and therefore the TVD property, we should have:
   $0 \leq \frac{\Delta x}{\Delta_- u_i}(u_{,x})_i \leq 1$ and $0 \leq \frac{\Delta x}{\Delta_+ u_i}(u_{,x})_i \leq 1$,
3. For neighbor points of an extreme u_i (with estimated derivative $(u_{,x})_i = 0$; this is based on condition 2), for uniform grids with width Δx, the neighbor derivatives meet conditions (see [60], example 2.4):
   $\frac{1}{2} \mid \frac{\Delta x}{\Delta_- u_i}(u_{,x})_{i-1} \mid \leq 1$ and $\frac{1}{2} \mid \frac{\Delta x}{\Delta_+ u_i}(u_{,x})_{i+1} \mid \leq 1$,

In these conditions, we have: $(u_x)_i$ denotes an estimation of the spatial derivative: $(u_x)_i := \frac{\mathrm{d}}{\mathrm{d}x}u(x_i)$; $u_i := u(x_i)$; $\Delta x_i := x_{i+1/2} - x_{i-1/2}$ denotes ith cell width; in case of uniform grids: $\Delta x = \Delta x_i$; $F^*_{i\pm1/2}$ represent reconstructed fluxes at right and left cell boundaries $x_{i\pm1/2}$; $\Delta_\pm u_i := \pm(u_{i\pm1} - u_i)$; $(u_{,x})_{i\pm1}$ are the estimated (limited) first derivatives at points $x_{i\pm1}$.

The conditions 1–3 have physical meaning; the first condition states that an extreme solution with maximum value should decrease in time (i.e., $u^{n+1}_i \leq u^n_i$), while an extreme solution with minimum value should increase through time (i.e., $u^{n+1}_i \geq u^n_i$). From the second condition, it is clear that at extreme points we must have: $(u_{,x})_i = 0$. Due to the third condition, the reconstructed values in cell edges should satisfy the monotonicity feature: magnitude of the reconstructed values should be less than immediately neighbor cell center values. This means, for example, if $u^n_{i-1} \leq u^n_i \leq u^n_{i+1}$, then $u^n_{i-1} \leq u^n_{i-1/2} \leq u^n_i \leq u^n_{i+1/2} \leq u^n_{i+1}$.

The third local TVD condition is for uniform cells; in case of non-uniform cells, due to the E-condition at extreme values u_i with estimated derivative $(u_{,x})_i = 0$, we have:

$$\mathrm{Sign}(u_{i+1} - u_i) = \mathrm{Sign}\left(\left\{\left(u_{i+1} - \frac{\Delta x_{i+1}}{2}(u_{,x})_{i+1}\right) - (u_i)\right\}\right),$$

$$\mathrm{Sign}(u_i - u_{i-1}) = \mathrm{Sign}\left(\left\{(u_i) - \left(u_{i-1} + \frac{\Delta x_{i-1}}{2}(u_{,x})_{i-1}\right)\right\}\right).$$

According to these relationships, TVD preserving derivatives should satisfy:

$$\frac{1}{2}\mid \frac{\Delta x_{i-1}}{\Delta_- u_i}(u_{,x})_{i-1}\mid \le 1 \qquad \text{and} \qquad \frac{1}{2}\mid \frac{\Delta x_{i+1}}{\Delta_+ u_i}(u_{,x})_{i+1}\mid \le 1$$

These two relationships confirm also as before necessity of the monotone reconstruction in cell edges for non-uniform cells.

7.2. Irregularity effects on slope limiters

The central/central-upwind schemes (e.g., the KT method) is originally developed for uniform cells. Most of them satisfy the TVD and monotonicity preserving conditions. On irregular cells, these methods do not completely meet these conditions and therefore do not remain necessarily stable. In the following, effects of cell irregularities will be studied by considering the monotonicity preserving necessity and the local TVD conditions.

It will be shown that only the grid modification (for gradual variation of grids) is not generally enough to guarantee TVD results.

7.2.1. Slope limiters on uniform grids

Most of slope limiters meet some necessary conditions, as: 1) the TVD; 2) preserving linear approximation; and 3) symmetric feature. These features are explained, in brief, as follows.

The TVD property. Considering physical meanings of the local TVD conditions 1–3, the upper limit of a TVD limiter for ith cell is (for more details, one can see [31]):

$$u_i' = \min\left\{\frac{2(\Delta_+ u_i)}{\Delta x}, \frac{2(\Delta_- u_i)}{\Delta x}\right\}, \tag{7.2}$$

where u_i denotes cell center solution on the ith cell and operator u_i' is upper limit of a discrete approximation of $grad(u_i)$ in a way that solutions remain TVD. To have TVD solutions, estimated derivative $(u_x)_i := du(x_i, t)/dx$ should be limited by a slope limiter $\phi_i := \phi(R_i)$ as $\phi_i(u_x)_i$. The function ϕ_i is a slope limiter at x_i, where $0 \le \phi_i \le 1$. Parameter R_i measures smoothness by relative of successive gradients around point x_i; for uniform grids its definition is: $R_i = \frac{\Delta_+ u_i/\Delta_+ x_i}{\Delta_- u_i/\Delta_- x_i} = \frac{\Delta_+ u_i}{\Delta_- u_i}$.

For all TVD slope limiters, it is necessary that: $\phi_i(u_x)_i \le u_i'$ (this upper TVD limiter will be derived on non-uniform cells).

Linear approximation preserving. This linearity preserving condition guarantees that linear solutions should not be limited. This is an important point to have a second order accuracy away from extrema. For a linear function with slope s on a uniform grid, it is clear: $R_i = \Delta_+ u_i/\Delta_- u_i = \{s.(\Delta_+ x_i)\}/\{s.(\Delta_- x_i)\} = 1$, where $s.(\Delta_+ x_i) := s(x_{i+1} - x_i)$ and $s.(\Delta_- x_i) := s(x_i - x_{i-1})$. In this regard, the linear preserving condition is: $\phi(1) = 1$. This constraint can also be obtained by considering the MINMOD limiter definition: the linear preserving feature is conserved if the forward and backward derivatives are the same, i.e., $R_i = 1$.

The symmetric feature. The condition is: $\phi(R_i) = \phi((1/R)_i)$. This condition assure that slope limiter effects are the same for forward and backward propagating solutions. To more clarify this feature, a new parameter f is defined as: $f = (\Delta_- u_i)/(\Delta_0 u_i)$, where $\Delta_0 u_i := u_{i+1} - u_{i-1}$. For monotone solutions, u_i is always between u_{i-1} and u_{i+1}, so f always belongs to the range [0, 1]. The parameters R and f have then a relationship with each other, as: $R = (1-f)/f$. The symmetric property is now clear, since: $\phi(f) = \phi(R) = \phi((1-f)/f)$ and $\phi(1/R) = \phi(f/(1-f)) = \phi(1-f)$, then $\phi(f) = \phi(1-f)$ for $0 \le f \le 1$.

7.3. Slope limiters on cell-centered non-uniform grids

A grid with non-uniform cells is considered. Widths of successive cells can be related to each other by coefficients: $a = \Delta x_{i-1}/\Delta x_i$ and $b = \Delta x_{i+1}/\Delta x_i$. Possible jump in solutions between points x_{j+1} and x_{j-1} is denoted by $\Delta_0 u_i$, where $\Delta_0 u_i := u_{i+1} - u_{i-1}$. The forward $(D_+ u_i)$, backward $(D_- u_i)$ and centered $(D_0 u_i)$ differences can then be written as: $D_\pm u_i := \frac{\Delta_\pm u_i}{\Delta_\pm x_i}$, $D_0 u_i := \frac{\Delta_0 u_i}{\Delta_- x_i + \Delta_+ x_i}$. Considering definition of f, these derivatives can be rewritten as: $D_+ u_i = (2(1-f)\Delta_0 u_i)/((1+b)\Delta x_i)$; $D_- u_i = (2f\Delta_0 u_i)/((1+a)\Delta x_i)$; and $D_0 u_i = (2\Delta_0 u_i)/((2+a+b)\Delta x_i)$.

The TVD property. This can be obtained by the local TVD conditions 1–3 (see [31]). It has the same definition as the uniform case (Eq. (7.2)):

$$u_i' = \min\left\{\frac{2\Delta_+ u_i}{\Delta x_i}, \frac{2\Delta_- u_i}{\Delta x_i}\right\}. \tag{7.3}$$

Linear approximation preserving. For non-uniform grids, the linear preserving condition for a slope limiter is [31]:

$$\phi_i D_i(f = f_p) = \frac{2\Delta_0 u_i}{(a+b+2)\Delta x_i},$$

where $f_p = \frac{a+1}{a+b+2}$. The linear preserving feature is conserved if the backward and forward derivatives are equal to each other: $D_+ u_i = D_- u_i$. By considering the MINMOD definition, this happens for case $f = f_p$, or values of $\phi_i D_i(f_p)$ are values of the MINMOD limiter at the f_p.

Symmetric condition. This feature is not fulfilled, in general.

7.4. Performance of the generalized MINMOD limiter on non-uniform grids

The generalized MINMOD (GMINMOD), can be rewritten as:

$$(\phi_i D_i)_{\text{GMINMOD}} = \text{GMINMOD}\{\theta D_- u_i, D_0 u_i, \theta D_+ u_i\}, \quad 1 \le \theta \le 2. \tag{7.4}$$

In case of non-uniform grids, different definitions of $D_0 u_i$ can be considered. One is based on the above-mentioned definition: $D_0 u_i = \Delta_0 u_i/(\Delta_- x_i + \Delta_+ x_i)$, and the other one obtains by the first order least square based estimated slope, as [31]:

$$D_0 u_i = D_{\text{Lsq.}} u_i := \frac{\Delta_+ x_i^2}{\Delta_- x_i^2 + \Delta_+ x_i^2} D_+ u_i + \frac{\Delta_- x_i^2}{\Delta_- x_i^2 + \Delta_+ x_i^2} D_- u_i. \tag{7.5}$$

On uniform grids, both definitions lead to the first order central difference equation: $(u_{i+1} - u_{i-1})/(2\Delta x_i)$. Performance of these two GMINMOD limiters will be illustrated on non-uniform grids.

Regarding f and $\Delta_0 u_j$ definitions, functions $D_{\text{Lsq.}} u_i$ (Eq. (7.5)) and u_i' (Eq. (7.3)) can be rewritten as:

$$D_0 u_i = D_{\text{Lsq.}} u_i = \frac{(1+b)(1-f) + (1+a)}{(1+b)^2 + (1+a)^2}\left\{\frac{f.\Delta_0 u_i}{\Delta x_i}\right\},$$

$$u_i' = \min\{f, 1-f\}\frac{2\Delta_0 u_i}{\Delta x_i},$$

where: $f := \frac{u_i - u_{i-1}}{u_{i+1} - u_{i-1}}$ and $\Delta_0 u_i := u_{i+1} - u_{i-1}$.

Performance of the GMINMOD limiters on uniform and non-uniform grids are shown in Fig. 5. Fig. 5(a) is for uniform case and Fig. 5(b) and (c) are for non-uniform cases. In all figures, center of each cell, x_i, is in the middle of ith cell, i.e.:$x_i = (x_{i+1/2} + x_{i-1/2})/2$. A gradual variation of cell lengths is considered for irregular grids. In Fig. 5(b) length of cells are: $\Delta x_{i-1} = 2\text{d}x$, $\Delta x_i = \text{d}x$, and $\Delta x_{i+1} = 0.5\text{d}x$; and in Fig. 5(c) the lengths are: $\Delta x_{i-1} = 2\text{d}x$, $\Delta x_i = 1.5\text{d}x$, and $\Delta x_{i+1} = \text{d}x$. The results confirm that: 1) on gradually varying grids, limiters may not completely remain in the TVD region; 2) the symmetry condition may not satisfy; 3) more gradual variation of grids is, more stability exists; 4) the long-term numerical stability cannot guarantee; and 5) the GMINMOD limiter by the direct-definition of central differencing, $D_0 u_i = (\Delta_0 u_i)/(\Delta_- x_i + \Delta_+ x_i)$, leads to more symmetric behaviors, so this definition will be considered in this work.

It will be shown that to have a TVD solution (defined on non-uniform grids) without modifying limiter definitions (the GMINMOD limiter, here), the cell middle point, x_i, should be shifted slightly; and this is only necessary for transmitting cells (a cell between two surrounding uniform cells with different cell lengths). In the following, at first, it will be shown how to choose properly cell centers/edges by the adaptive wavelet transform. It will then mathematically be proved that why such spatial configurations lead to stable and TVD solutions without modifying limiter definitions.

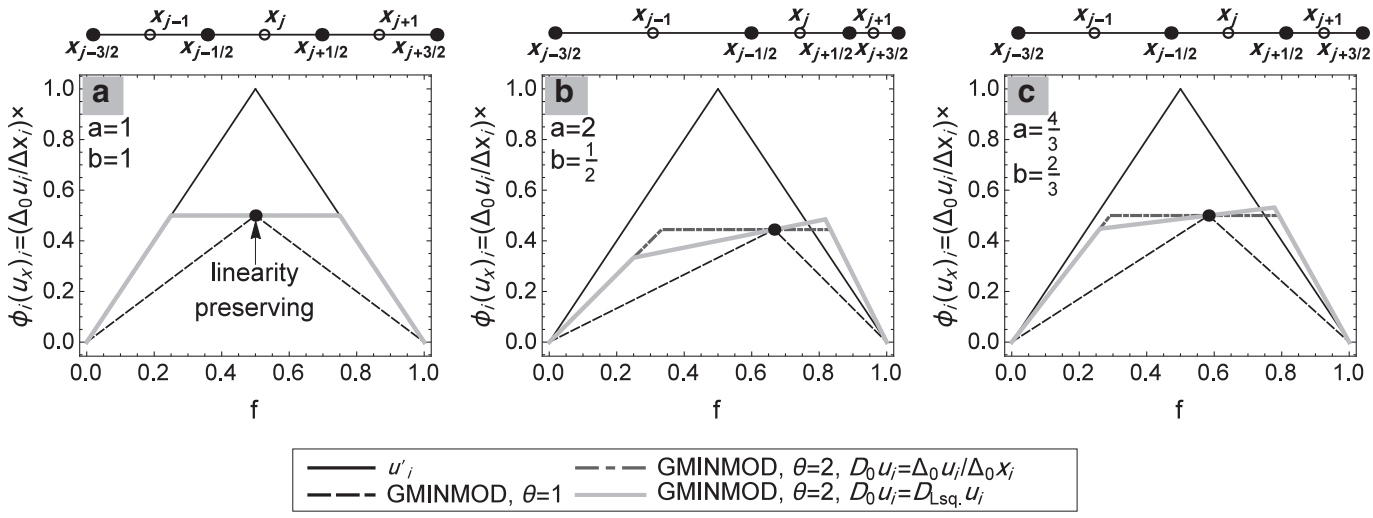

Fig. 5. Performance of GMINMOD limiters on non-uniform grids. Regarding the top row in each figure, hollow circles and solid points represent center of cells and cell edges, respectively.

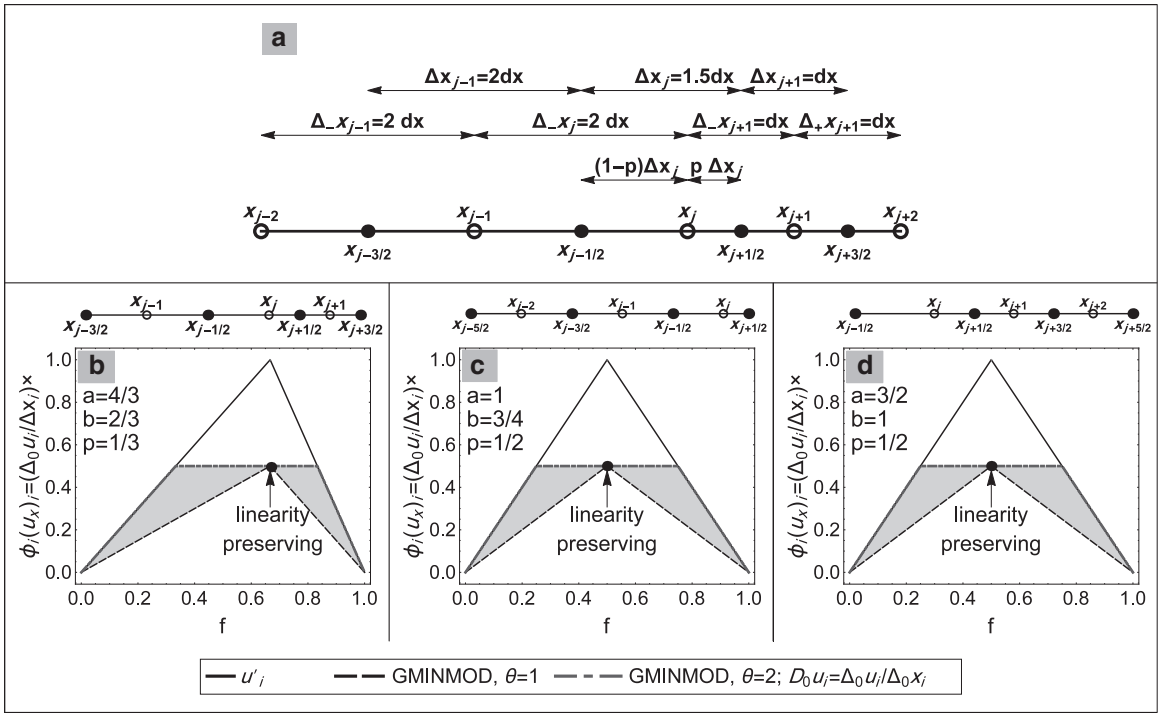

Fig. 6. Wavelet based adaptive distribution of cell centers x_j, corresponding edge locations and TVD feature of the GMINMOD limiter on resulted non-uniform grids.

7.5. Choosing of cell centers and edges by the wavelet-based adaptation algorithm

In this work, at first, cell center positions, x_j, are evaluated by the adaptive wavelet transform, and then, cell edges are simply assumed to be the middle point of them, as: $x_{j+1/2} = (x_j + x_{j+1})/2$.

The interpolating wavelet theory in Section 2 uses the pyramid algorithm. In this formulation, distance between detail coefficients in the resolution j is twice those in the resolution $j+1$. Let us consider an adapted grid where for every adapted points of resolution level $j+1$, there always exist two surrounding adapted points of resolution level j. For such adapted grids, inter-distances of successive points increase or decrease gradually by the dyadic pattern. Let us consider an adapted cell-centers as $\{\ldots, 2\mathrm{d}, 2\mathrm{d}, \mathrm{d}, \mathrm{d}, \ldots\}$. This means, for grid points $\{\ldots, x_{j-2}, x_{j-1}, x_j, x_{j+1}, x_{j+2}, \ldots\}$, we have: $x_{j-1} - x_{j-2} = x_j - x_{j-1} = 2\mathrm{d}x$ and $x_{j+1} - x_j = x_{j+2} - x_{j+1} = \mathrm{d}x$. Such configuration is illustrated in Fig. 6(a). For this adapted points, it is assumed that there always exist three successive points with equal distances from each other. In this figure, cell edges are middle point of two successive cell centers, i.e.: $x_{j+1/2} = (x_j + x_{j+1})/2$. By this, length of created cells are: $\{\ldots, \Delta x_{j-1} = 2\mathrm{d}x, \Delta x_j = 1.5\mathrm{d}x, \Delta x_{j+1} = \mathrm{d}x, \ldots\}$. Note that jth cell acts as a transiting cell with a shifted cell center (x_j is no longer in the middle of cell j). In all the surrounding cells, all cell centers remain in the middle of cells. In the next subsection, it will be proved that such cell configuration leads to stable and TVD results. This cell configuration can obtain by the post-processing stage, Section 3.

7.6. Stability and TVD conditions on wavelet-based adapted grids

In the proposed wavelet-based grid adaptation, as mentioned, cell center of transmitting cells do not remain in the middle of cells, Fig. 6(a). In Fig. 6, three pattern of successive cells are distinguishable: 1) $\{j-2, j-1, j\}$; 2) $\{j-1, j, j+1\}$; and 3) $\{j, j+1, j+2\}$. These sets are shown in Fig. 6 (b)–(d). In the set (2), the transmitting cell j is in the middle, while in the remaining groups, the transmitting cell j is the first or the last cell.

In the following, the TVD local conditions are checked and modified for such spatially non-centered cell centers. This will be done for the set (2) (see Fig. 6(b)), and then it will be checked for the groups (1) and (3).

7.6.1. The TVD condition when transmitting cell is in the middle of surrounding cells (the set (2))

To provide the TVD condition for the cell set $\{j-1, j, j+1\}$ (see Fig. 6(b)), a right propagating scalar advection equation is considered as: $u_t + \bar{a}u_x = 0$ for $\bar{a} > 0$. For simplicity, the forward Euler discretization in time will be used. The upwind finite volume method with second order accuracy will be considered for the spatial discretization. The resulted discretized system is:

$$u_j^{n+1} = u_j^n - \frac{\bar{a}\Delta t}{\Delta x_j}\left(u^L_{j+\frac{1}{2}} - u^L_{j-\frac{1}{2}}\right). \tag{7.6}$$

The symbol L represents the upwind flux and therefore the upwind-based reconstructed value of $u^L_{j+1/2}$ is:

$$u^L_{j+\frac{1}{2}} = u_j + \left(p\Delta x_j\right)S_j,$$

where $S_j := \phi_j D_j$ is a limited slope at point x_j. Let us assume in the transmitting cell j, the cell center x_j locates in a way that $x_{j+1/2} - x_j = p\Delta x_j$ and $x_j - x_{j-1/2} = (1-p)\Delta x_j$. For the wavelet based adapted grids, it is easy to show that $p = 1/3$.

To show a method is TVD, it should be confirmed that: 1) a monotone increasing (or decreasing) solution remains monotone increasing (or decreasing) in time (the monotonicity preserving feature: resulted from the posivity condition [60]); 2) if u_j^n is a local maximum (or minimum), then at the next time step: $u_j^{n+1} \le u_j^n$ (or $u_j^{n+1} \ge u_j^n$) (due to the first local TVD condition).

Controlling of the monotonicity preserving condition. Assume a monotonically increasing solution at time step $t = t^n$ as: $u^n_{j-1} \le u^n_j \le u^n_{j+1}$. This feature should satisfy at the next time step, i.e.: $u^{n+1}_{j-1} \le u^{n+1}_j \le u^{n+1}_{j+1}$.

For the monotone increasing solution $\left\{u_j^n\right\}$, slopes S_{j-1} and S_j are positive, so: $u^n_{j-1/2} = u^n_{j-1} + (\Delta x_{j-1}/2)S_{j-1} \le u^n_j$ and $u^n_{j+1/2} = u^n_j + (p\Delta x_j)S_j \ge u^n_j$. These inequalities are obtained due to the monotone reconstruction constraint: the local TVD condition 3. Hence from Eq. (7.6), we have:

$$u_j^{n+1} \le u_j^n - \frac{\bar{a}\Delta t}{\Delta x_j}\left(u_j^n - u_j^n\right) = u_j^n. \tag{7.7}$$

To complete the proof, we need to estimate a below bound for u_j^{n+1}. At first, due to the local TVD constraint on reconstruction edge values (the condition 3), it is clear that: $u_j^n - (1-p)\Delta x_j S_j \ge u^n_{j-1}$. By considering this relationship, and conditions $S_j \ge 0$ & $S_{j-1} \ge 0$, from Eq. (7.6), we have:

$$\begin{aligned} u_j^{n+1} &= u_j^n - \lambda_j\left(\left(u_j^n + \left(p\Delta x_j\right)S_j\right) - \left(u^n_{j-1} + \left(\frac{\Delta x_{j-1}}{2}\right)S_{j-1}\right)\right) \\ &\ge u_j^n - \lambda_j\left(\left(u_j^n + \left[u_j^n - u^n_{j-1} - \Delta x_j S_j\right]\right) - \left(u^n_{j-1}\right)\right) \\ &\ge u_j^n - \lambda_j\left(\left(u_j^n + u_j^n - u^n_{j-1}\right) - \left(u^n_{j-1}\right)\right) = u_j^n(1-2\lambda_j) + 2\lambda_j u^n_{j-1}, \end{aligned}$$

so:

$$u_j^{n+1} \ge u^n_{j-1}, \tag{7.8}$$

where $\lambda_j := \bar{a}\Delta t/\Delta x_j$. The relationship (7.8) valids for $\lambda_j \le 0.5$. Eqs. (7.7) and (7.8) lead to the condition $u^{n+1}_{j-1} \le u^n_{j-1} \le u^{n+1}_j \le u^n_j \le \cdots$. This means a monotone solution remains monotone through time.

Controlling of the extreme conditions (the first local TVD condition).

1. *Local maximum:* let us have a right propagating wave, $\bar{a} > 0$ and u^n_{j+1} is a local maximum on the group cell (2) (Fig. 6(b)). Due to the extreme condition, we have: 1) $S_{j+1} = 0$ (the second local TVD condition); 2) $u^n_{j+1} \ge u^n_j$ and $u^n_{j+1} \ge u^n_{j-1}$; and 3) $S_j \ge 0$ (due to the monotone reconstruction feature). Rewriting Eq. (7.6) for the maximum point, we have:

$$\begin{aligned} u^{n+1}_{j+1} &= u^n_{j+1} - \frac{\bar{a}\Delta t}{\Delta x_{j+1}}\left(u^L_{j+\frac{3}{2}} - u^L_{j+\frac{1}{2}}\right) \\ &= u^n_{j+1} - \frac{\bar{a}\Delta t}{\Delta x_{j+1}}\left(\left[u^n_{j+1} + 0.5\Delta x_{i+1}S_{j+1}\right] - \left[u^n_j + p\Delta x_j S_j\right]\right) \\ &= u^n_{j+1} - \frac{\bar{a}\Delta t}{\Delta x_{j+1}}\left(\left[u^n_{j+1}\right] - \left[u^n_j + p\Delta x_j S_j\right]\right). \end{aligned}$$

To guarantee that $u^{n+1}_{j+1} \le u^n_{j+1}$, the term in the parentheses should be non-negative; hence:

$$0 \le S_j \le \frac{u^n_{j+1} - u^n_j}{p\Delta x_j} = \frac{\Delta_+ u^n_j}{p\Delta x_j}. \tag{7.9}$$

2. *Local minimum* let us assume the wave propagate to the left, $\bar{a} < 0$ and u^n_{j-1} is a local minimum. This means: $u^n_{j-1} \le u^n_j$, $u^n_{j-1} \le u^n_{j-2}$, $S_{j-1} = 0$ and $S_j \ge 0$. By the spatio-temporal discretization (7.6) at x_{j-1}, we have:

$$\begin{aligned} u^{n+1}_{j-1} &= u^n_{j-1} - \frac{\bar{a}\Delta t}{\Delta x_{j-1}}\left(u^L_{j-\frac{1}{2}} - u^L_{j-\frac{3}{2}}\right) \\ &= u^n_{j-1} - \frac{\bar{a}\Delta t}{\Delta x_{j-1}}\left(\left[u^n_j + (1-p)\Delta x_j S_j\right] - \left[u^n_{j-1} + 0.5\Delta x_{j-1}S_{j-1}\right]\right) \\ &= u^n_{j-1} - \frac{\bar{a}\Delta t}{\Delta x_{j-1}}\left(\left[u^n_j + (1-p)\Delta x_j S_j\right] - \left[u^n_{j-1}\right]\right). \end{aligned}$$

Since $\bar{a} < 0$ and due to the constraint $u^{n+1}_{j-1} \ge u^n_{j-1}$, we should have: $\left(\left[u^n_j + (1-p)\Delta x_j S_j\right] - \left[u^n_{j-1}\right]\right) \ge 0$. This means:

$$0 \le S_j \le \frac{u^n_j - u^n_{j-1}}{(1-p)\Delta x_j} = \frac{\Delta_- u^n_j}{(1-p)\Delta x_j}. \tag{7.10}$$

From Eqs. (7.9) and (7.10), the TVD constraint on non-uniform grids is:

$$S_j = u'_j = \min\left\{\frac{\Delta_- u^n_j}{(1-p)\Delta x_j}, \frac{\Delta_+ u^n_j}{p\Delta x_j}\right\}. \tag{7.11}$$

7.6.2. The TVD condition when transmitting cell is the first or last cell (the set (1) or (3))

In this case, it is easy to show that the TVD limiter constraint, u'_j is the same as cell-centered cells, see Eq. (7.3).

7.6.3. Linearity preserving condition

To preserve the linearity preserving condition, and so the second order accuracy of solutions away from extrema, limiters should satisfy:

$$\left(\phi_j D_j\right)(f = f_p) = \frac{2}{a+b+2}\frac{\Delta_0 u_j}{\Delta x_j}, \tag{7.12}$$

where: $f_p := \frac{2+a-2p}{2+a+b}$ and $\Delta_0 u_j := u_{j+1} - u_{j-1}$. The point f_p corresponds to the location where the common MINMOD limiter (*MM*) reaches its maximum value. On non-uniform grids, it is easy to show that:

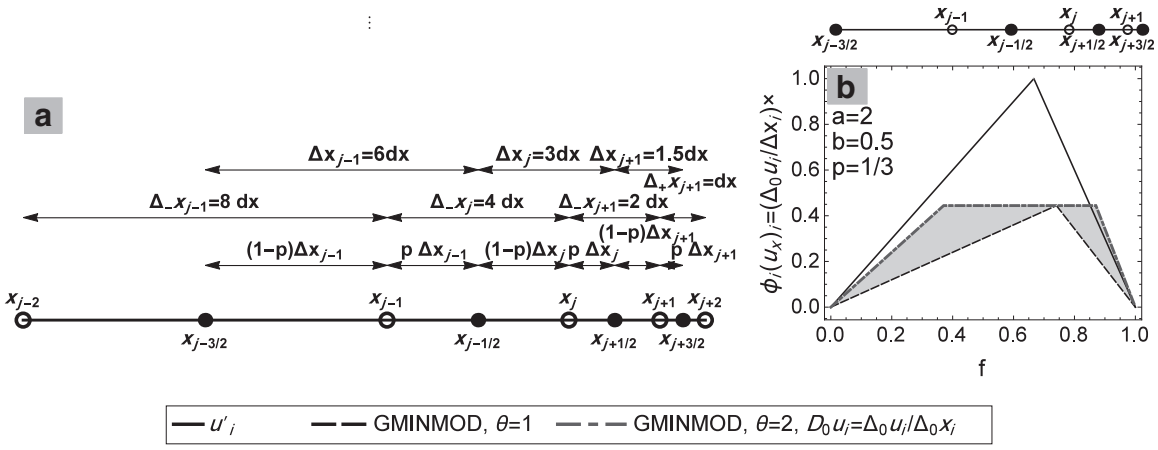

Fig. 7. Effects of weaker restriction on wavelet-based grid variation. For this figure, we assume $x_{j+1}-x_j=0.5(x_j-x_{j-1})$; a) cell configurations; b) the GMINMOD limiter performance.

$$(\phi_j D_j)_{MM} := \min\left\{\frac{\Delta_- u_j}{\left[(1-p_j)+\frac{a}{2}\right]\Delta x_j}, \frac{\Delta_+ u_j}{\left[p_j+\frac{b}{2}\right]\Delta x_j}\right\} = \min\left\{\frac{f}{\left[(1-p_j)+\frac{a}{2}\right]}, \frac{1-f}{\left[p_j+\frac{b}{2}\right]}\right\}\frac{\Delta_0 u_j}{\Delta x_j}. \tag{7.13}$$

So: $(\phi_j D_j)_{MM}(f=f_p)=\frac{2}{a+b+2}\frac{\Delta_0 u_j}{\Delta x_j}$.

7.7. Controlling of the TVD condition for slope limiters on wavelet-based adapted grids

A modified wavelet-based adapted grid is considered; the modification is performed by the post-processing stage. It is assumed also there always exists at least three neighbor cell centers of equal distances from each other, as explained in Section 7.5 and illustrated in Fig. 6(a). In this figure, we have: $x_{j-1}-x_{j-2}=2\mathrm{d}x$, $x_j-x_{j-1}=2\mathrm{d}x$, $x_{j+1}-x_j=\mathrm{d}x$ and $x_{j+2}-x_{j+1}=\mathrm{d}x$. This configuration of grid points leads to stable and TVD solutions, which will be studied later. Depending of the transmitting cell location, three cell sequences are detectable: 1) $\{j-2,j-1,j\}$; 2) $\{j-1,j,j+1\}$; 3) $\{j,j+1,j+2\}$ (Fig. 6(a)).

Cell sequence $\{j-1,j,j+1\}$: *Transmitting cell j (with a shifted cell center) is the middle one.* In this case, we have $\Delta_- x_j=[a/2+(1-p)]\Delta x_j$ and $\Delta_+ x_j=[p+b/2]\Delta x_j$. So, the backward, forward and central derivatives (in the GMINMOD limiter, Eq. (7.4)) can be rewritten as: $D_- u_j=\frac{2f\Delta_0 u_j}{[a+2(1-p)]\Delta x_j}$, $D_+ u_j=\frac{2(1-f)\Delta_0 u_j}{[2p+b]\Delta x_j}$, and $D_0 u_j=\frac{2\Delta_0 u_j}{(2+a+b)\Delta x_j}$. Where $a:=\Delta x_{j-1}/\Delta x_j=4/3$ & $b:=\Delta x_{j+1}/\Delta x_j=2/3$; p measures cell-center shifting and here $p=1/3$ (see Fig. 6(a) and (b)).

The functions S_j (u'_j) (Eq. (7.11)) and GMINMOD (Eq. (7.4)) are illustrated in Fig. 6(b). The comparison offers: 1) the limiter remains completely in the TVD region; 2) the linear preserving feature is satisfied; 3) at the expense of the symmetric feature, the transmitting cell j acts properly for joining surrounding cells; and 4) shifting of the cell center leads to a TVD result (Fig. 6(b)), while cell-centered one does not (Fig. 5(c)).

Cell sequence $\{j-2,j-1,j\}$ *(see Fig. 6(c))* In this case, we have: $\Delta_- x_j=(1+a)\frac{\Delta x_j}{2}$ and $\Delta_+ x_j=[1+2b(1-p)]\frac{\Delta x_j}{2}$. Hence: $D_- u_j=\frac{2f\Delta_0 u_j}{(1+a)\Delta x_j}$, $D_+ u_j=\frac{2(1-f)\Delta_0 u_j}{[1+2b(1-p)]\Delta x_j}$ and $D_0 u_j=\frac{2\Delta_0 u_j}{(2+a+2(1-p)b)\Delta x_j}$; where $a=1$, $b=3/4$ and $p=1/3$. Definition of the S_{j-1} (or u'_{j-1}) is the same as the uniform case, Eq. (7.3). Comparison of this limiter with the GMINMOD is shown in Fig. 6(c). It is obvious, the GMINMOD limiter remains in the TVD region.

Cell sequence $\{j,j+1,j+2\}$ *(see Fig. 6(d))* Here we have: $\Delta_- x_j=\frac{(1+2ap)\Delta x_j}{2}$ and $\Delta_+ x_j=\frac{(1+b)\Delta x_j}{2}$. Hence $D_- u_j=\frac{2f\Delta_0 u_j}{(1+2ap)\Delta x_j}$, $D_+ u_j=\frac{2(1-f)\Delta_0 u_j}{(1+b)\Delta x_j}$ and $D_0 u_j=\frac{2\Delta_0 u_j}{(2+2ap+b)\Delta x_j}$; where $a=3/2$, $b=1$ and $p=1/3$. The function S_{j+1} (or u'_{j+1}) is the same as the uniform case. This function is compared with the GMINMOD limiter in Fig. 6(d), where stable and TVD results are attached.

In General, it can be concluded that on irregular grid points with typical grid configuration illustrated in Fig. 6(a), numerical solutions will remain TVD and thereby stable.

7.8. Constraint on cell center adaptation in the wavelet-based algorithm

As mentioned before, it is always assumed that there exist at least three neighbor cell centers of equal distance from each other in non-uniform adapted cell centers. Let us assume an adapted cell with a weaker cell-sequence condition: $x_{j+1}-x_j=0.5(x_j-x_{j-1})$ or $x_{j+1}-x_j=2(x_j-x_{j-1})$. As an example let us consider:

$x_{j-1}-x_{j-2}=8\mathrm{d}x, x_j-x_{j-1}=4\mathrm{d}x, x_{j+1}-x_j=2\mathrm{d}x$ and $x_{j+2}-x_{j+1}=\mathrm{d}x$ (Fig. 7(a)). For this case, if cell edges are assumed to be in the middle of cell centers, $x_{j+1/2}=0.5(x_j+x_{j+1})$, then cell lengths are: $\Delta x_{j-1}=6\mathrm{d}x, \Delta x_j=3\mathrm{d}x$ and $\Delta x_{j+1}=1.5\mathrm{d}x$. Hence: $\Delta_- x_j=[(1-p)+ap]\Delta x_j$, $\Delta_+ x_j=[p+(1-p)b]$, $D_- u_j=\frac{f\Delta_0 u_j}{[(1-p)+ap]\Delta x_j}$, $D_+ u_j=\frac{(1-f)\Delta_0 u_j}{[p+(1-p)b]\Delta x_j}$, and $D_0 u_j=\frac{\Delta_0 u_j}{[1+ap+b(1-p)]\Delta x_j}$; where $a=2$ and $b=0.5$. For all cells, shifting coefficient is equal to $p=1/3$ (see Fig. 7(a)).

The GMINMOD (Eq. (7.4)) and u'_j (from non-uniform cases: Eq. (7.11)) are compared in Fig. 7(b). It is clear that the limiter is slightly outside the TVD domain. For this reason, long term stability of numerical solutions could vanish. For cell-centered cases, where $x_j=(x_{j+1/2}+x_{j-1/2})/2$, the results are not also TVD, see Fig. 5(b).

To have stable results, cell centers are located in a way that there always exist at least three neighbor grids (cell centers) of equal distance from each other. To guarantee this condition, in the grid modification stage (the post-processing stage), it is assumed, at least, to have: $N_s=N_c=1$.

8. Numerical examples

The following examples are to study the effectiveness of the proposed method concerning nonlinear 1-D and 2-D first order hyperbolic systems. The main assumptions are: 1- applying the D-D interpolating wavelet of order 3; 2- using the generalized MINMOD flux/slope limiter in all problems; 4- repeating re-adaptation processes every time step;

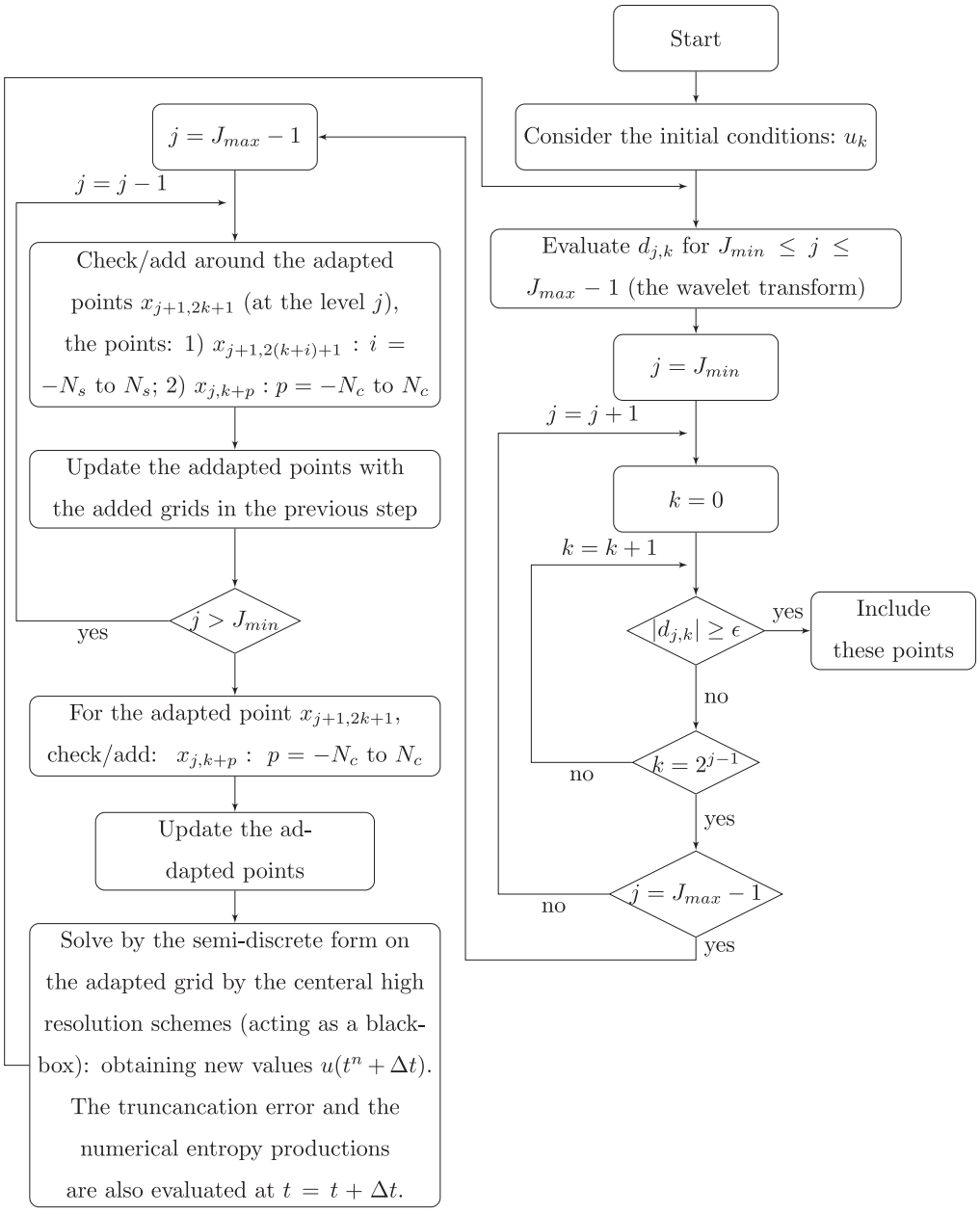

Fig. 8. The MRA-based algorithm for the simulation of hyperbolic problems.

5- using the semi-discrete form of central and central-upwind schemes;
6- integrating in time by the TVD Runge–Kutta second-order solver.

Fig. 8 summarizes the MRA-based simulation by the central schemes (for 1-D problems).

8.1. Burgers' equation

This is the simplest model to simulate nonlinear advection. It appears in different applied mathematics, for instance nonlinear acoustics, fluid mechanics and traffic flow.

The Burgers equation is defined as follows:

$$u_t + \frac{1}{2}(u^2)_x = 0,$$

where u is the conserved quantity and its flux is $F(u) = u^2/2$. The system is nonlinear, so that discontinuous fronts will develop during front propagations. Here it is assumed that the initial and boundary conditions are:

$$\text{BCs}: \ u(x=0,t) = u(1,t) = 0, \qquad \text{IC}: \ u(x,t=0) = \sin(2\pi x) + \frac{1}{2}\sin(\pi x).$$

For the above conditions, a discontinuity starts to appear around $t \approx 0.158$. This discontinuous front will propagate to the right side after this time. Assumptions for the numerical simulations are: $\epsilon = 10^{-3}$ (threshold), $\theta = 2$ (the flux limiter parameter), $N_c = N_s = 2$ (for the post-processing stage), $J_{max} = 11$, and $J_{min} = 5$. The numerical results are illustrated in Fig. 9 at times 0.158, 0.5, and 1. This figure contains numerical results, exact solutions and corresponding adapted grids in different resolutions. The results confirm that adapted points are properly concentrated around propagating fronts.

8.1.1. Some comparisons with other MRA-based adaptive methods

In the following, the results of the adaptive KT scheme are compared with: i) The adaptive NVSF method [14]; ii) The adaptive essentially nonoscillatory-Roe (ENO-Roe) scheme [62,63]; iii) The adaptive

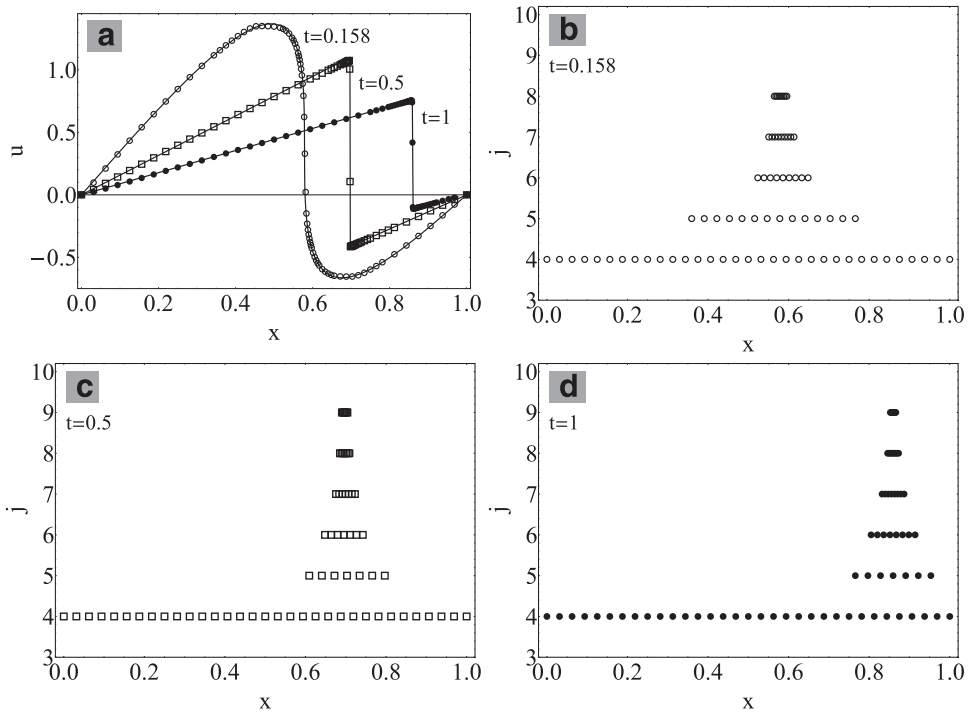

Fig. 9. The Burgers' solution and corresponding adapted grid points (in figure (a), exact solutions are presented by the solid line and numerical solutions are illustrated by points and hollow shapes).

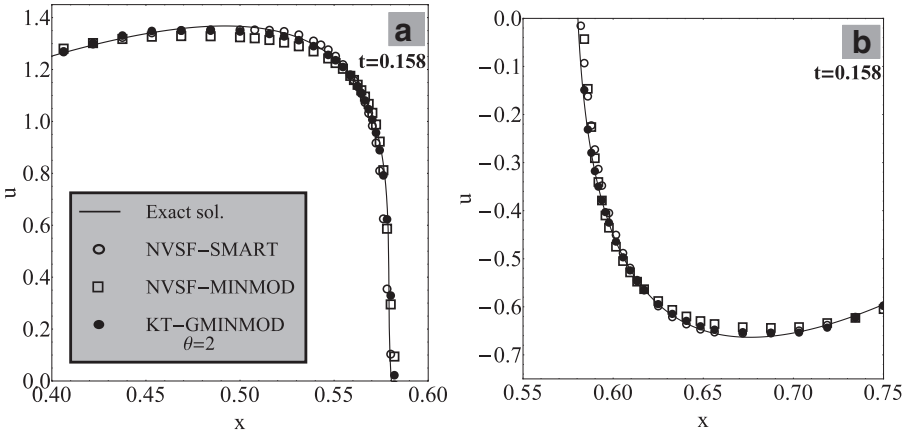

Fig. 10. Comparison of the proposed adaptive central method and NVSF-based upwind scheme.

scheme proposed by Holmström [64] by the integration of central finite difference (FD) schemes with the sparse point representation (SPR) of solutions (SPR-FD).

i) The adaptive NVSF. The KT central scheme and NVSF-based method [14] are compared on wavelet-based adapted grids (the NVSF-based method is basically developed for non-uniform grid points). The values of the parameters are: $\epsilon = 10^{-3}$, $\theta = 2$ (for GMM in the KT scheme), $N_c = N_s = 2$, $J_{max} = 11$ and $J_{min} = 5$. The *second* order TVD Runge–Kutta method is used for the time integration. The results are presented in Fig. 10 at time 0.158. For the NVSF formulation, two types of flux limiters are considered: the SMART and MINMOD limiters [14]. The results offer that the proposed method is comparable with the schemes originally provided for non-uniform grid points.

ii) The adaptive ENO-Roe scheme. Both the adaptive KT and ENO-Roe methods are simulated with the parameters: $\epsilon = 10^{-2}$, $N_c = N_s = 1$, $J_{max} = 12$ and $J_{min} = 4$. For the KT scheme, it is assumed: $\theta = 2$ (for the GMM). For both methods, the time integration is performed by the *third-order* TVD Runge–Kutta method.

Adaptive and exact solutions are presented in Fig. 11 at $t = 0.158, 0.5$ and 1; in these illustrations, markers $\circ$ and $\times$, and the solid line show the solutions obtained by the ENO-Roe, the KT and the exact method, respectively. It is obvious that results from two adaptive methods have a good agreement (the KT method is slightly more dissipative than the ENO-Roe scheme; see the solutions at $t = 0.158$).

iii) The SPR-FD scheme proposed by Holmström [64]. In this benchmark, a Burgers' equation with a diffusion term is considered, as:

$$u_t + \frac{1}{2}\left(u^2\right)_x = Q^x\left(u, u_x\right)_x, \tag{8.1}$$

where here $Q^x\left(u, u_x\right) = \mu u_x$ is the diffusion term, in which $u_x := \partial u/\partial x$ and μ is a constant. The BCs and IC are assumed to be:

$$\text{BCs}: \; u(x=0,t) = u(1,t) = 0, \qquad \text{IC}: \; u(x,t=0) = \sin(2\pi x). \tag{8.2}$$

The semi-discrete form of Eq. (8.1) is:

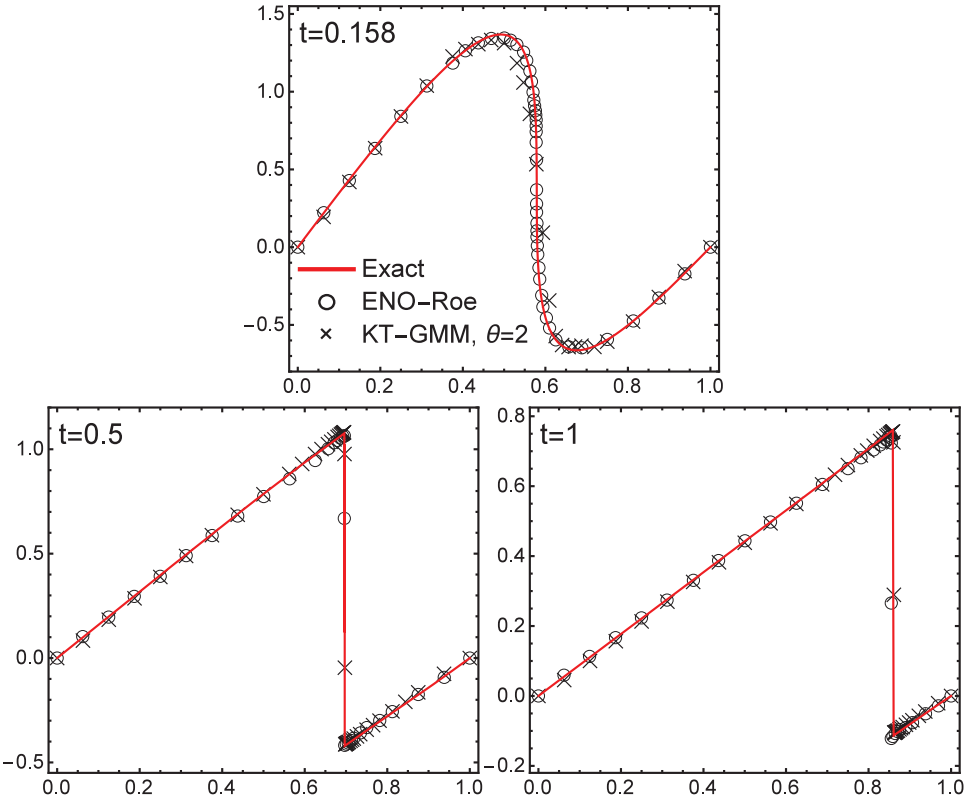

Fig. 11. The comparison between the adaptive KT and ENO-Roe [62] schemes on MRA-based adapted grids at $t = 0.158$, 0.5 and 1.

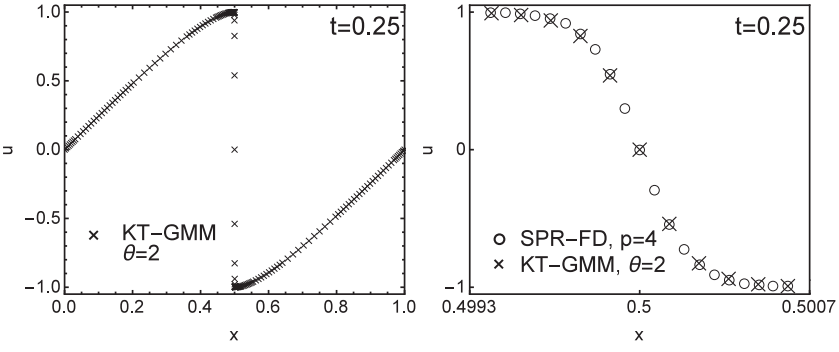

Fig. 12. The comparison between the adaptive KT and SPR-FD [64] schemes on MRA-based adapted grids at $t = 0.25$.

$$\frac{du_i}{dt} + \frac{F^*_{i+1/2} - F^*_{i-1/2}}{\Delta x_i} = \frac{P_{i+1/2} - P_{i-1/2}}{\Delta x_i}, \tag{8.3}$$

where

$$P_{i-1/2} = \frac{1}{2}\left\{ Q(u_{i-1}, \frac{u_i - u_{i-1}}{\Delta x_{i-1}} + Q(u_i, \frac{u_i - u_{i-1}}{\Delta x_{i-1}} \right\},$$
$$P_{i+1/2} = \frac{1}{2}\left\{ Q(u_i, \frac{u_{i+1} - u_i}{\Delta x_i} + Q(u_{i+1}, \frac{u_{i+1} - u_i}{\Delta x_i} \right\}. \tag{8.4}$$

In this study, the assumed parameters are: $\mu = 10^{-4}$, $\epsilon = 10^{-5}$, $\theta = 2$, $J_{max} = 14$ and $J_{min} = 4$ [64]. For the KT scheme, the third-order TVD Runge–Kutta method is used for the time integration; for the SPR-FD method, the common fourth-order Runge–Kutta method is used for the time integration and spatial derivatives are approximated by the centered finite difference method stencil of order $p = 4$. A discontinuity develops in the solution of Eq. (8.1) at $x = 0.5$ which obtains its maximum at $t = 0.25$. The adaptive solutions are presented in Fig. 12 at $t = 0.25$. The zoomed in solutions reveal that both solutions can properly resolve the discontinuity.

8.2. Euler system of equations

For this system, the governing equation is:

$$\frac{\partial}{\partial t}\begin{pmatrix} \rho \\ \rho u \\ E \end{pmatrix} + \frac{\partial}{\partial x}\begin{pmatrix} \rho u \\ \rho u^2 + P \\ u(E+P) \end{pmatrix} = \begin{pmatrix} 0 \\ 0 \\ 0 \end{pmatrix},$$

where ρ, u and E are gas density, velocity and total energy, respectively. The pressure P can be obtained by: $P = (\gamma - 1)\left(E - \frac{\rho u^2}{2}\right)$, where γ is the ratio of specific heats, and here it is assumed to be $\gamma = 1.4$.

In the following three different problems with different initial and boundary conditions will be studied. These diverse conditions lead to different bench-mark problems; they are: 1) the Sod problem [65]; 2) the Lax problem [66]; 3) Interaction of an entropy sine wave with a Mach 3 right-moving front [67].

8.2.1. Sod problem

This problem was developed for studying the performance of different numerical methods. It is a long gas tube divided into two equal parts with a diaphragm; each part contains gas with different features. Its solution includes, from right to left, a *shock* wave, a *contact discontinuity*

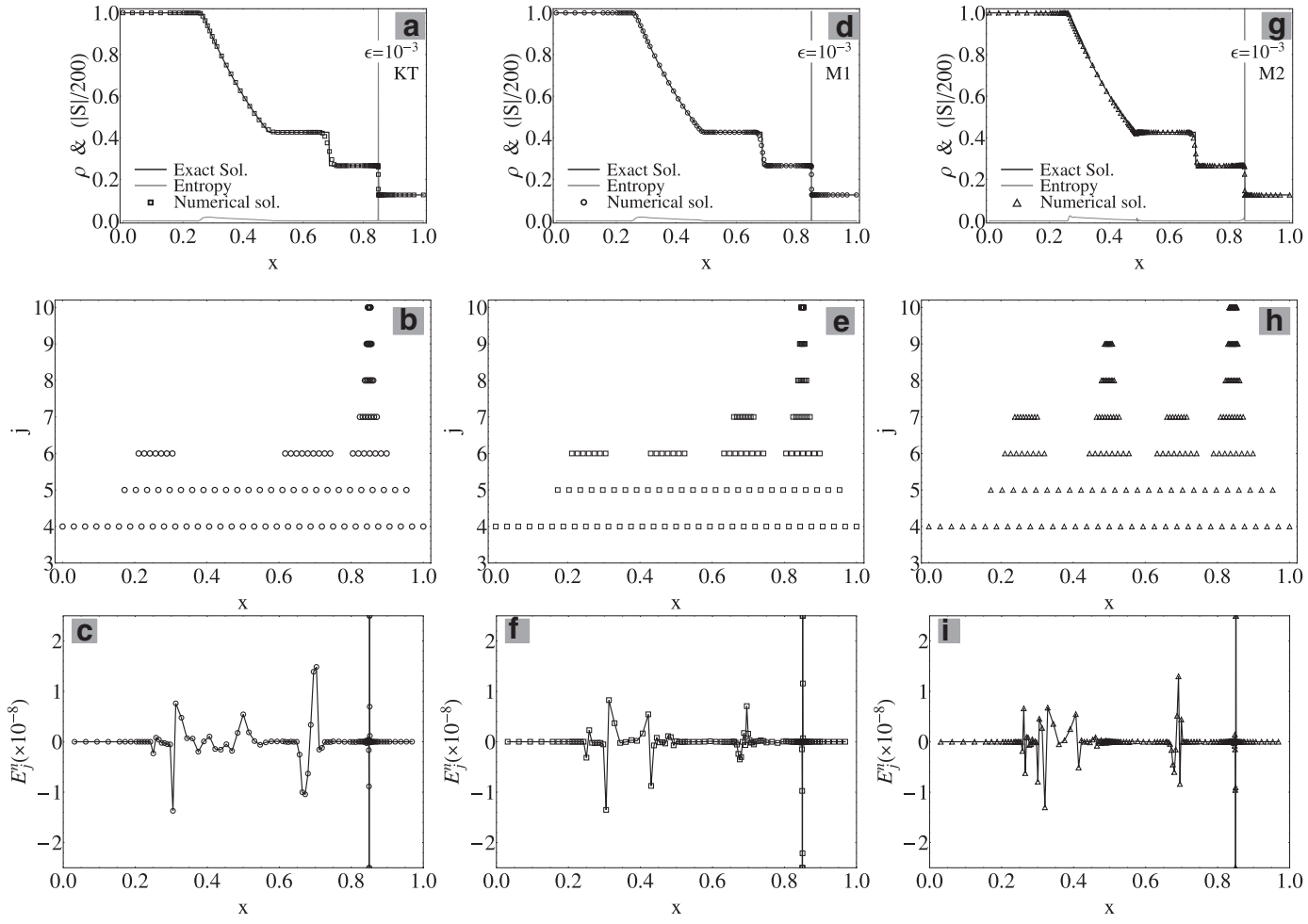

Fig. 13. Numerical results, corresponding truncation errors, entropy productions, and adapted points in different resolutions for the Sod problem with the KT, $M1$ & $M2$ schemes at $t = 0.2$; a–c) the KT scheme; d–f) the $M1$ method; g–i) the $M2$ scheme.

(the second discontinuity in the $\rho(t)$) and an *expansion zone or rarefaction wave*. In which, the expansion gas is separated from compressing gas by the contact discontinuity, and the rarefaction wave is a continuous process that the high pressure gas flows to the low pressure domain.

For the Sod problem, the initial conditions are:

$$\begin{pmatrix} \rho \\ u \\ P \end{pmatrix}_{t=0} = \begin{cases} \{0,0,1\}^T, & x \le 0.5, \\ \{0.125,0,0.1\}^T, & x > 0.5, \end{cases}$$

An unbounded 1-D domain is assumed: a Riemann problem. Assumptions for numerical simulations are: $J_{max} = 11$, $N_d = 6$, $\epsilon = 10^{-3}$, $\theta = 2$, $N_c = 2$, $N_s = 1$ and $dt = 10^{-5}$. The numerical solutions and corresponding adapted grid points are illustrated in Fig. 13 at time 0.2 with methods KT, $M1$ and $M2$. For the KT method, results are presented in Fig. 13(a)–(c); these figures contains numerical results, corresponding entropy productions (S_j^n), adapted grids and local truncation errors (E_j^n). These results for the $M1$ and $M2$ schemes are provided respectively in Fig. 13(d)–(f) and (g)–(i).

Fig. 13 provides that: 1) methods $M1$ & $M2$ have less numerical dissipation in comparison with the KT scheme; 2) the $M2$ scheme leads to the smallest dissipation; 3) using a less dissipative method, more grid points concentrate automatically in different resolutions. This is confirmed by comparing N_g values of these three methods during simulations, see Figs. 13(b),(e),(h) and 14.

The numerical entropy production cannot detect the contact discontinuity in this example (Fig. 13(a),(d) & (g)), even by less dissipative methods with fine enough resolutions. Entropies S_j^n have small values in the rarefaction zone (for $0.25 < x < 0.45$), but can properly detect shock waves. The local truncation error can capture both the shock wave and contact discontinuity. The local errors E_j^n have considerable values in rarefaction zones. This zone is not detected by the wavelet theory; as a result, grid points do not adapted there. Considering the wavelet-based adapted points, results of S_j^n, and E_j^n, different criteria lead to different adapted grids. In this example, it seems that wavelet-based adaptation method leads to more realistic adapted grids.

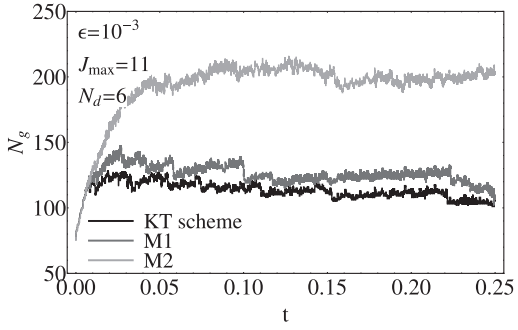

Fig. 14. Number of adapted grid points N_g during simulations. In the finest resolution, number of grid points is $2^{11} + 1$.

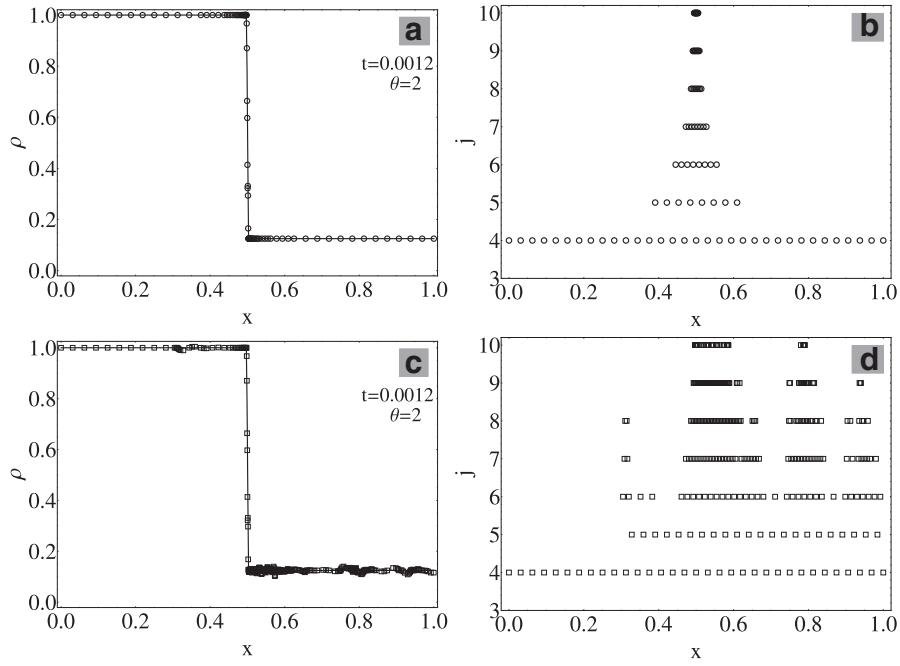

Fig. 15. Post-processing effects on stability of solutions; a–b) with the post-processing stage; c–d) without the post-processing step. In figures (a) & (c), solid lines and hollow shapes are exact and numerical solutions, respectively.

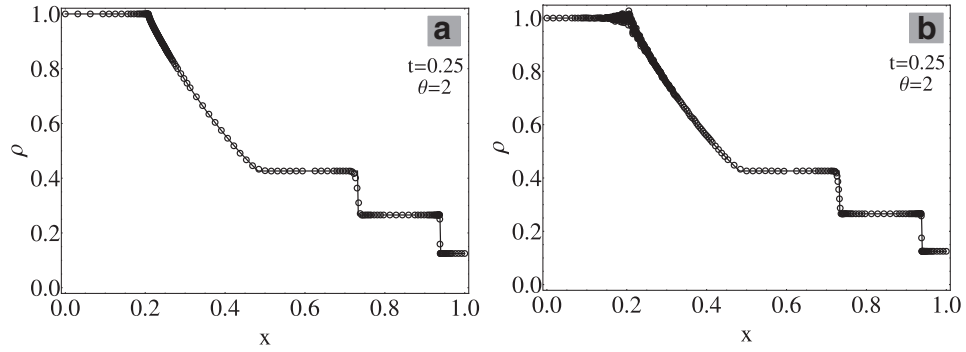

Fig. 16. Full and semi post processing effects; a) full post processing, $N_s = N_c = 2$; b) semi-post processing, $N_s = 2, \& N_c = 0$. Solid lines and hollow shapes are exact and numerical solutions, respectively.

Effects of the post-processing stage are investigated by some numerical simulations in the following. At first, effect of considering the post-processing stage is studied. Two simulations with and without the post-processing stage are done and results are presented in Fig. 15. Fig. 15(a)-(b) and (c)-(d) include solutions with and without the post-processing step, respectively. The results indicate that post-processing adapted grids have significant effects on solution stability. The numerical instability grows rapidly in absence of the post-processing step.

The post-processing stage contains both grid modification in the same resolution and successive coarser resolution, see Section 3. To study effects of them, two types of modifications are considered: full and partial grid modification (by a post-processing). The modifications are: 1) partial post processing: for a grid point having resolution j, new points are only added at the corresponding resolution level; here we assume: $N_s = 2$ & $N_c = 0$; 2) full post processing: both resolution level j and $j+1$ are controlled; we choose: $N_s = 2$ & $N_c = 1$. The former, the semi-modification, is frequently used in wavelet-based adaptation procedures. Numerical results are presented in Fig. 16. Fig. 16(a) and (b) correspond to methods using the full and partial post-processing stages, respectively. This figure shows that long-term stability can be obtained in case of having full-modification, Fig. 16(a).

8.2.2. Lax problem

In the solution of this problem, from right to left, a shock wave, a contact discontinuity and a rarefaction zone are developed. Amplitude of the shock wave and the contact discontinuity are larger than those of the Sod problem. In brief, the Sod and the Lax problems are used as benchmarks with the different values of shock waves, contact discontinuities and rarefaction zones.

The initial conditions of this problem are:

$$\begin{pmatrix} \rho \\ u \\ P \end{pmatrix}_{t=0} = \begin{cases} \{0.445, 0.69887, 3.5277\}, & x \le 0.5, \\ \{0.5, 0, 0.571\}, & x > 0.5, \end{cases}$$

and the problem is a Riemann problem. For simulations, it is assumed: $\epsilon = 10^{-3}$, $\theta = 2$, and $dt = 10^{-5}$.

For the three methods KT, $M1$ and $M2$, solutions ρ, corresponding entropies S_j^n, adapted grids, and truncation errors E_j^n are presented in Fig. 17 at time 0.16. Same as the Sod problem, the results offer that: 1) less dissipative methods mobilize more adapted grid points of fine resolutions; 2) numerical entropy production of these methods cannot detect the contact discontinuity; 3) the local truncation errors E_j^n can detect the contact discontinuity zones; 4) E_j^n can also detect rarefaction zones; 5) the wavelet transform can properly capture all phenomena: shock waves, rarefaction and contact discontinuity zones.

8.2.3. Interaction of an entropy sine wave with a Mach 3 right-moving front

This challenging problem was developed to reveal high order scheme capabilities by Shu and Osher [67].

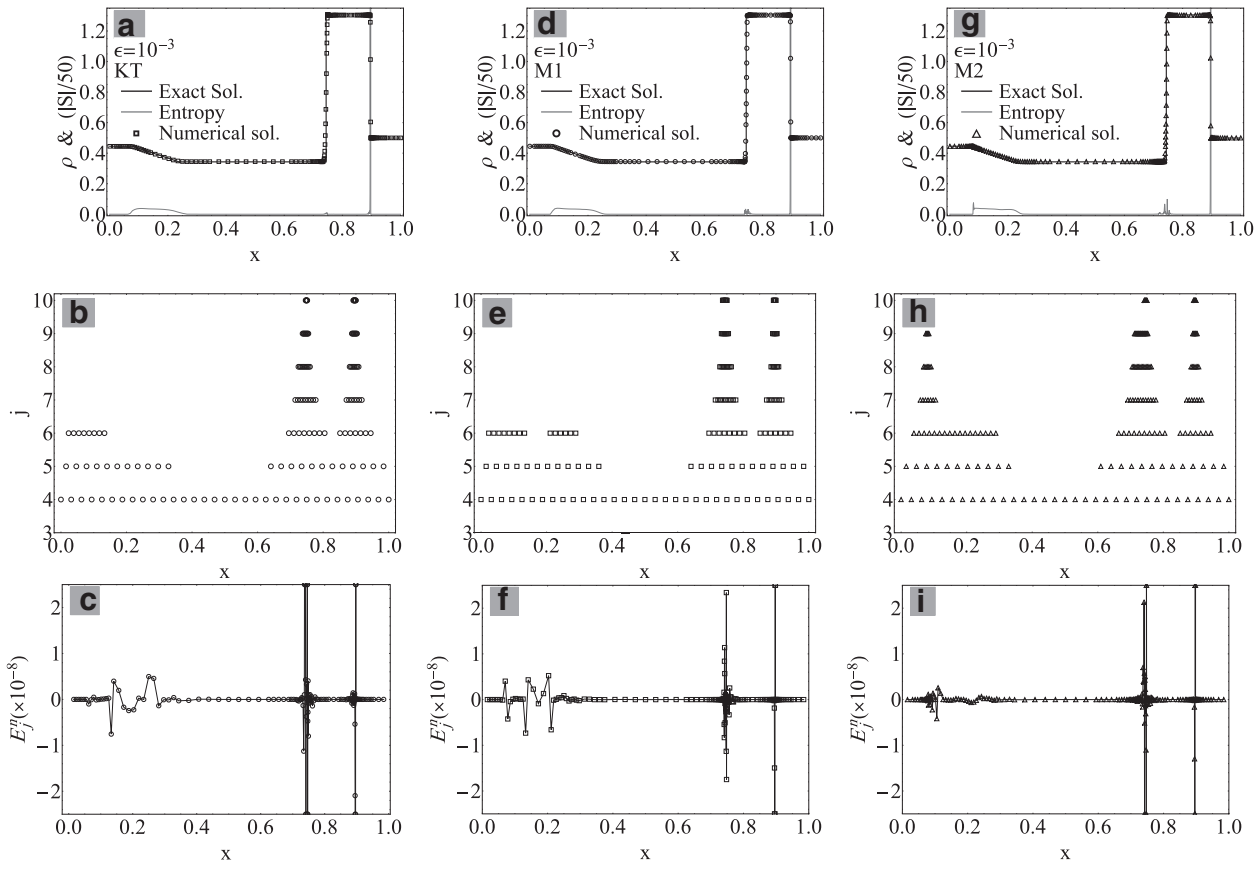

Fig. 17. Numerical results, corresponding entropy production, truncation errors, and adapted points of different resolutions for the Lax problem at $t = 0.1$; a–c) the KT scheme; d–f) the $M1$ method; g-i) the $M2$ scheme.

This problem is important due to the simulation of the shock-turbulence interactions. Amplified high-frequency entropy waves develop after the shock. These high frequency waves can be captured with numerical schemes with low numerical dissipation. Hence, this problem is a challenging benchmark to study the performance of numerical methods in: 1) Simulation of shock-turbulence interactions, 2) Handling of high frequency waves.

Here, it is assumed the ratio of specific heats is $\gamma = 1.4$. The Riemann initial condition is [67,68]:

$$\begin{pmatrix} \rho \\ u \\ P \end{pmatrix}_{t=0} = \begin{cases} \{3.857143, 2.629369, 10.33333\}, & x < -4, \\ \{1 + 0.2\sin(5x), 0, 1\}, & x \geq -4. \end{cases}$$

The considered computational domain is: $\Omega \in (-5, 5) \times (0, T)$; Assumed parameters are: $\epsilon = \epsilon_0 = 5 \times 10^{-3}$, $J_{max} = 11$, $J_{min} = 5$ (or $N_d = 6$), $N_c = 1$, $Ns = 2$, $\theta = 2$, $dt = 0.00025$.

The numerical entropy production, numerical and exact solutions are illustrated in Fig. 18 at $t = 1.8$. There, the solid lines and hollow shapes are the reference [68] and numerical solutions, respectively. Regarding numerical entropy productions, it is clear that both the $M1$ and $M2$ methods lead to less numerical dissipation in comparison to the KT scheme. The $M2$ scheme leads to the least dissipative results, since magnitude of entropy S is larger than both the KT and $M1$ methods. Distribution of adapted points at different resolution levels for these three schemes are shown in Fig. 19 at $t = 1.8$. The methods $M1$ and $M2$ lead to more adapted points of high resolutions. In Fig. 20 local truncation errors for these three methods are presented, which confirm numerical convergence.

8.3. 2-D Euler equation of gas dynamics for ideal gases

The governing equation for the 2-D system is:

$$\mathbf{u}_t + \mathbf{F}_x + \mathbf{G}_y = \mathbf{0},$$

where state values are $\mathbf{u} = \{\rho, \rho u, \rho v, E\}^T$; the flux vectors in the x and y directions are $\mathbf{F} = \left\{\rho u, \rho u^2 + P, \rho uv, u(E + P)\right\}^T$ and $\mathbf{G} = \left\{\rho v, \rho uv, \rho v^2 + P, v(E + P)\right\}^T$, respectively.

In this example, radially symmetric initial conditions are assumed with respect to the origin which it forms a dense localized high-pressure gas with zero initial velocity. There exists initial higher density and higher pressure inside a circle with radios $r = 0.4$; corresponding values are: $\left\{\rho_{in} = 1, \rho_{out} = 0.1\right\}$ & $\left\{P_{in} = 1, P_{out} = 0.1\right\}$. Other initial values are: $u_{in} = u_{out} = v_{in} = v_{out} = 0$ [39,69]. The computation domain belongs to $\Omega \in [-1.5, 1.5] \times [-1.5, 1.5]$. To control the symmetric of solutions and corresponding adapted grids in simulations, the total of the computing domain Ω is considered in simulations. Due to the symmetric initial conditions, the exact solutions are symmetric with respect to the origin. This feature can be used to control the performance of high resolution solvers.

The numerical results are presented in Fig. 21 at $t = 0.4$. Fig. 21(a) and (b) are from the KT scheme and Fig. 21(c) and (d) belong to the $M1$ method. The results offer that: 1) The result of the M1 method is more symmetric which confirms its better behavior, 2) Due to the numerical dissipation, the KT solver leads to slightly different result from the $M1$ one. To clarify the numerical dissipation effects, cut of solutions are compared along $y = 0$, Fig. 22. This figure confirms that the KT scheme leads to more dissipative results.

The local truncation errors E_j^n for the two schemes (KT and $M1$) and corresponding adapted grids are presented in Fig. 23 at $t = 0.2$. It

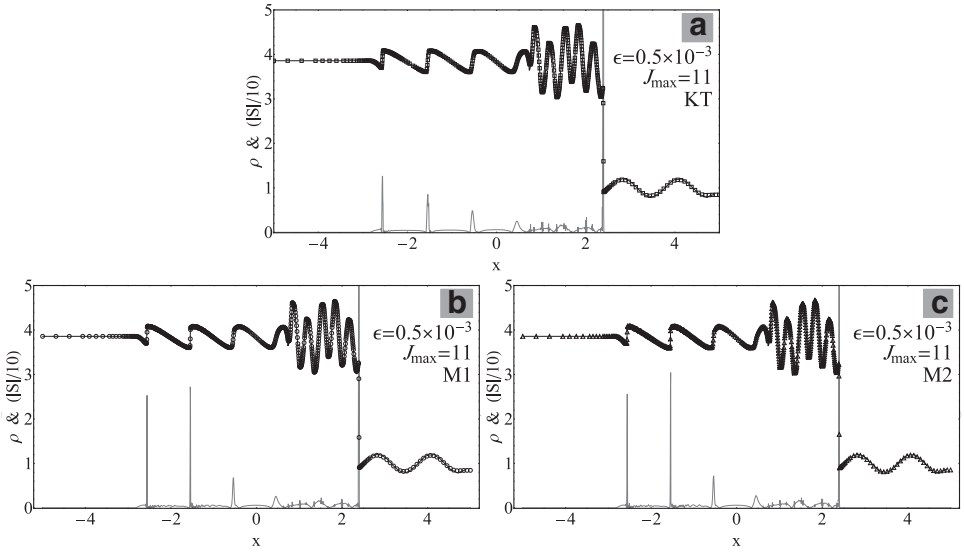

Fig. 18. Numerical results, and entropy productions for the right propagating front with the KT, *M*1 & *M*2 schemes at $t = 1.8$. In these figures, solid black lines are the reference solutions, hollow shapes are numerical ones, and the gray solid lines are numerical entropy productions.

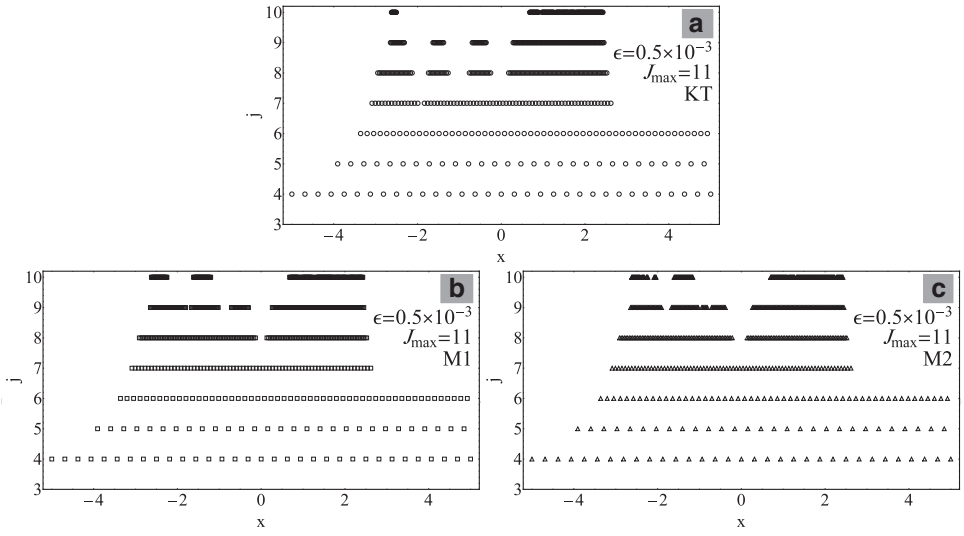

Fig. 19. Distribution of adapted grid points in different levels of resolution for the KT, *M*1 & *M*2 schemes at $t = 1.8$.

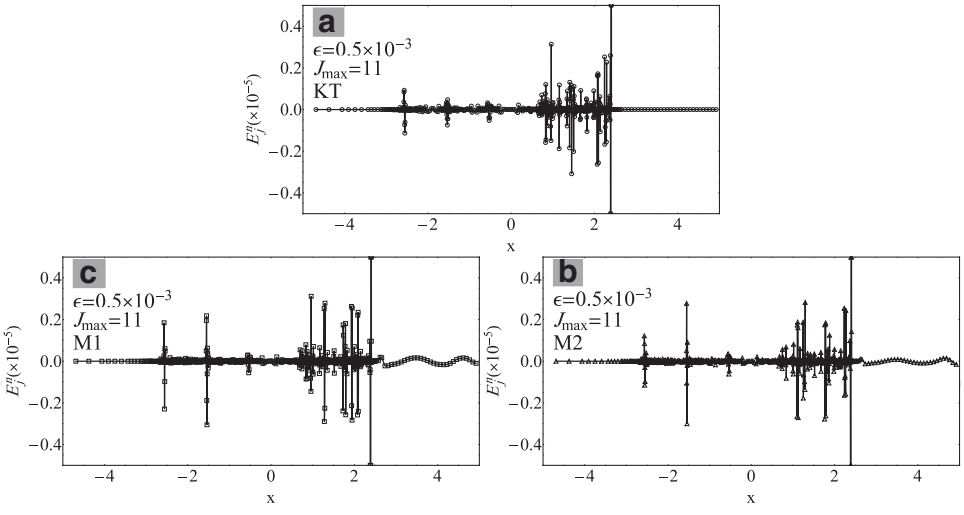

Fig. 20. Local truncation errors for the right propagating front with the KT, *M*1 & *M*2 schemes at $t = 1.8$.

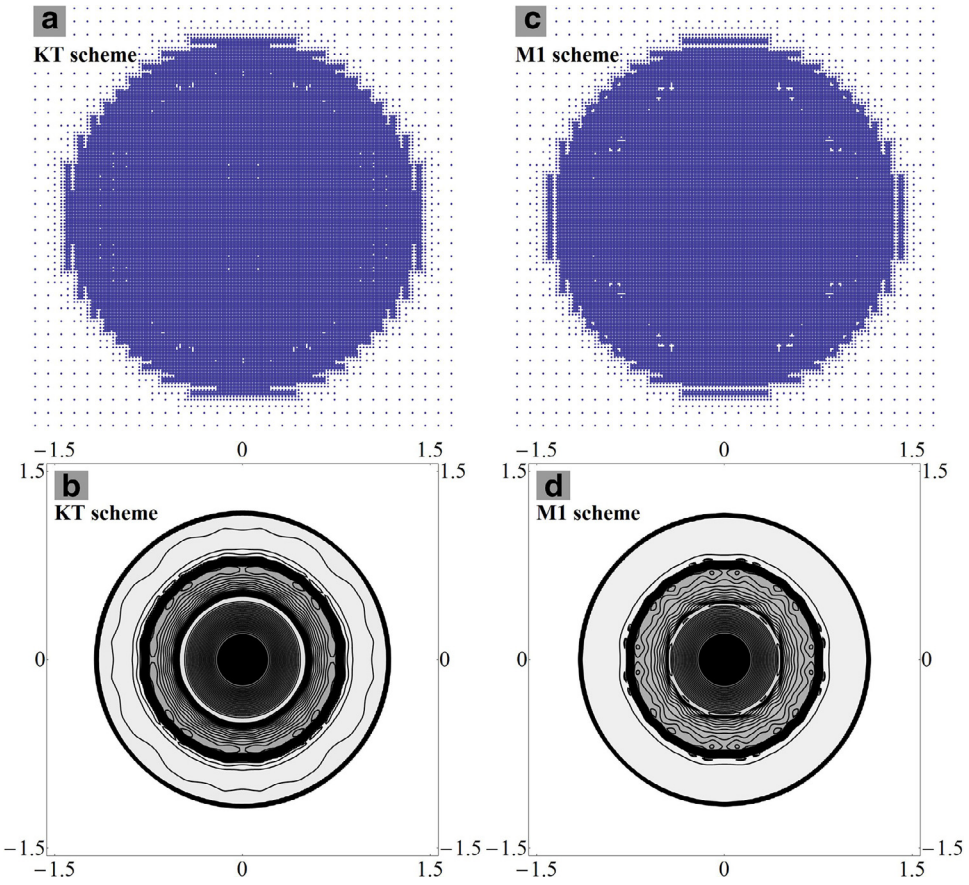

Fig. 21. The 2-D Euler gas dynamic adaptive solutions with corresponding adapted grids at $t = 0.4$.

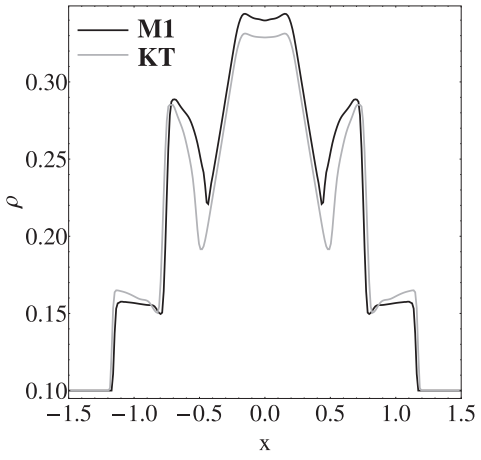

Fig. 22. Comparison of numerical results obtained by the KT and $M1$ schemes along $y = 0$ at $t = 0.4$.

is clear that the errors are properly concentrated in high-gradient zones detected properly by the wavelet transform.

8.4. A non-convex example: the polymer system

The governing equation of the polymer system is:

$$\frac{\partial}{\partial t}\begin{pmatrix} s \\ b \end{pmatrix} + \frac{\partial}{\partial x}\begin{pmatrix} f(s,c) \\ c f(s,c) \end{pmatrix} = \begin{pmatrix} 0 \\ 0 \end{pmatrix}, \tag{8.5}$$

where s denotes water saturation; parameter c is the polymer concentration; function $f := f(s, c)$ presents the fractional flow function of water; parameter b is function of s and c where $b := b(s, c)$. Functions b and f are assumed to be: $b(s,c) = sc + a(c)$ and $f(s,c) = \frac{s^2}{s^2+(0.5+c)(1-s)^2}$, where $a(c)$ denotes the adsorption function and in this example, it is: $a(c) = \frac{c}{5(1+c)}$. The exact solution of this problem is complex and contains both simple and composite waves which makes it challenging for numerical solvers [39].

The eigenvalues of the polymer system (8.5) are: $\lambda_1 = f_s(s,c)$ and $\lambda_2 = f(s,c)(s + a'(c))^{-1}$.

For numerical simulations, we assume: $J_{max} = 11$, $N_d = 6$, $\epsilon = 10^{-4}$, $dt = 0.00025$, and $N_s = N_c = 1$ (for grid modification).

In numerical simulations two types of θ are assumed: constant and adaptive. In adaptive case, in this work, it is assumed θ depends linearly on spatial positions of cell centers x_j, as:

$$\theta(x_j) = 1 + \frac{\{(\Delta x_j + \Delta x_{j+1})/2\} - \Delta x_{min}}{\Delta x_{max} - \Delta x_{min}}, \qquad \theta_j := \theta(x_j),$$

where $\Delta x_j := x_j - x_{j-1}$, $\Delta x_{min} := \min\{\Delta x_j\}$, and $\Delta x_{max} := \max\{\Delta x_j\}$. So, around high-gradient solutions $\theta \to 1$ and in smooth regions $\theta \to 2$. To study resolution effect, this example is also re-simulated for a fine resolution with resolution number: $J_{max} = 13$. In this case, number of decomposition levels is $N_d = 8$ and the time step is chosen in such a way that the CFL number does not change.

Numerical results and corresponding local truncation errors for the parameter s are illustrated in Fig. 24. The results provide that: 1) for case $\theta = 2$, the numerical solution does not converge to real one, even though it is a converged weak solution (Fig. 24(b)); 2) by using an adaptive scheme with adaptive θ, the result is nearly in accordance with the real solution, Fig. 24(c); by increasing J_{max} values (or using finer resolutions), the numerical solution approaches to the reference one, Fig. 24(e); 4) all of the results are the converged weak solutions due to errors E_j^n; 5) using more higher resolution level J_{max}, smaller local truncation errors are.

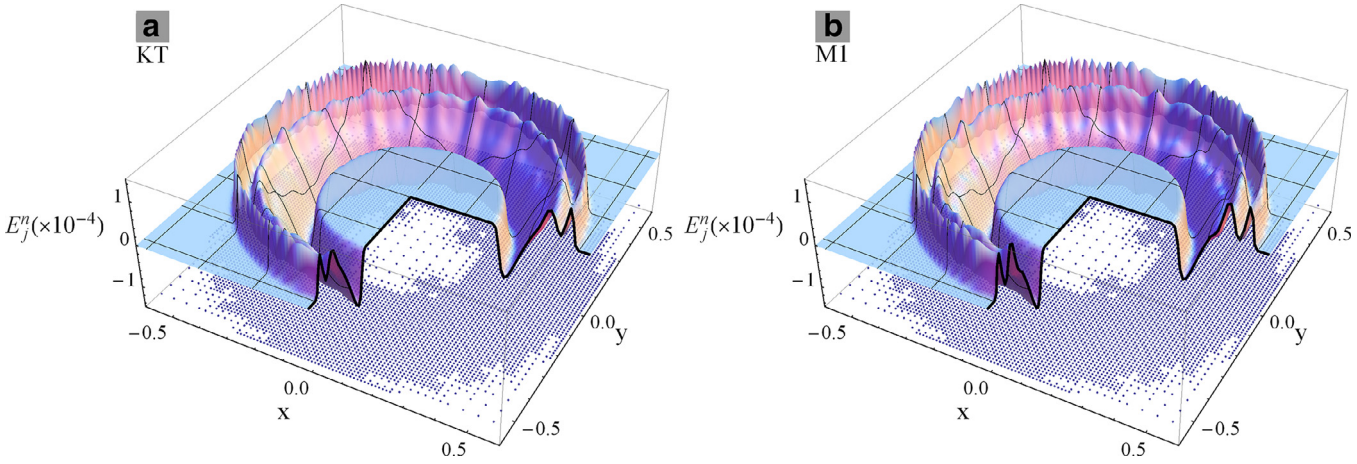

Fig. 23. Local truncation errors for the KT and $M1$ schemes at $t = 0.214$.

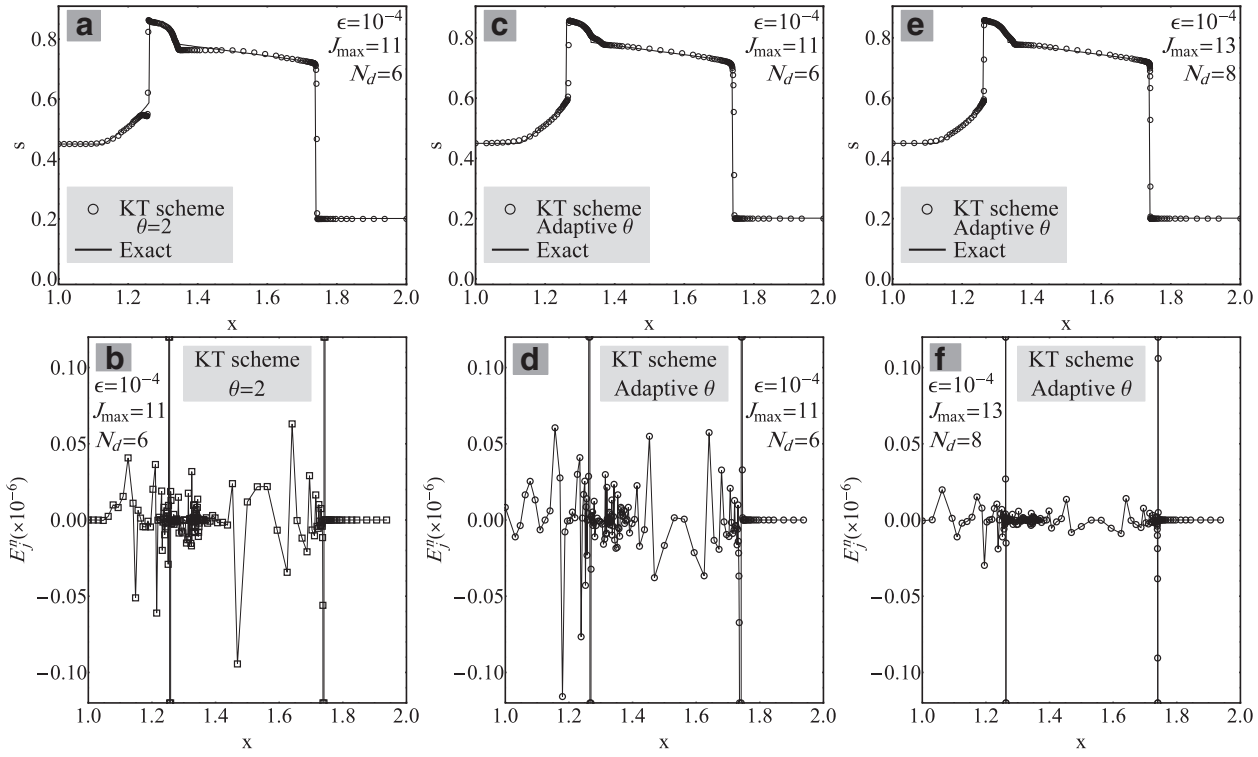

Fig. 24. Numerical solutions, corresponding adapted grids and local truncation errors for the polymer system; a, b) with $\theta = 2$; c,d) with adaptive θ; e,f) adaptive θ.

8.5. 2-D scalar conservation laws with non-convex fluxes

Let us assume a rotating wave with non-convex fluxes, defined as:

$$u_t + \{\sin(u)\}_x + \{\cos(u)\}_y = 0,$$

where $u := u(x, y, t)$ and the initial condition is:

$$u(x, y, t = 0) = \begin{cases} \frac{14\pi}{4}, & x^2 + y^2 < 1, \\ \frac{\pi}{4}, & x^2 + y^2 \geq 1. \end{cases}$$

This benchmark test, originally proposed in [39], is a challenging 2-D problem for many high resolution schemes due to the developing of 2-D composite waves in its solution.

For numerical simulations, we have: $J_{max} = 8$, $J_{min} = 5$ (or $N_d = 3$), $\epsilon = 10^{-4}$, $dt = 0.5 \times 10^{-3}$, and $N_s = N_c = 1$ (for the modification of adapted grid). For modeling, two different choices of θ are assumed: 1) the constant one with value $\theta = 2$; 2) the adaptive implementation of θ. The latter is also based on the 1-D linear interpolation of θ on adapted grid points, as:

$$\theta(Z_j) = 1 + \frac{\left(\Delta Z_{ave}\right)_j - \Delta Z_{min}}{\Delta Z_{max} - \Delta Z_{min}},$$

where $\left(\Delta Z_{ave}\right)_j := \left\{\left(\Delta Z_j + \Delta Z_{j+1}\right)/2\right\}$, $\Delta Z_j := Z_j - Z_{j-1}$, $Z_j \in \{x_j, y_j\}$, $\Delta Z_{max} = 1/2^{J_{min}}$, and $\Delta Z_{min} = 1/2^{J_{max}}$. For each direction, $\theta(Z_j)$ is calculated independently.

The numerical results and corresponding adapted grid points are shown in Fig. 25 at $t = 1$. Figures (a) and (b) correspond to the θ-adaptive results and figures (c) and (d) are from the constant θ. Again the θ-adaptive solver converges to proper and physical results [39].

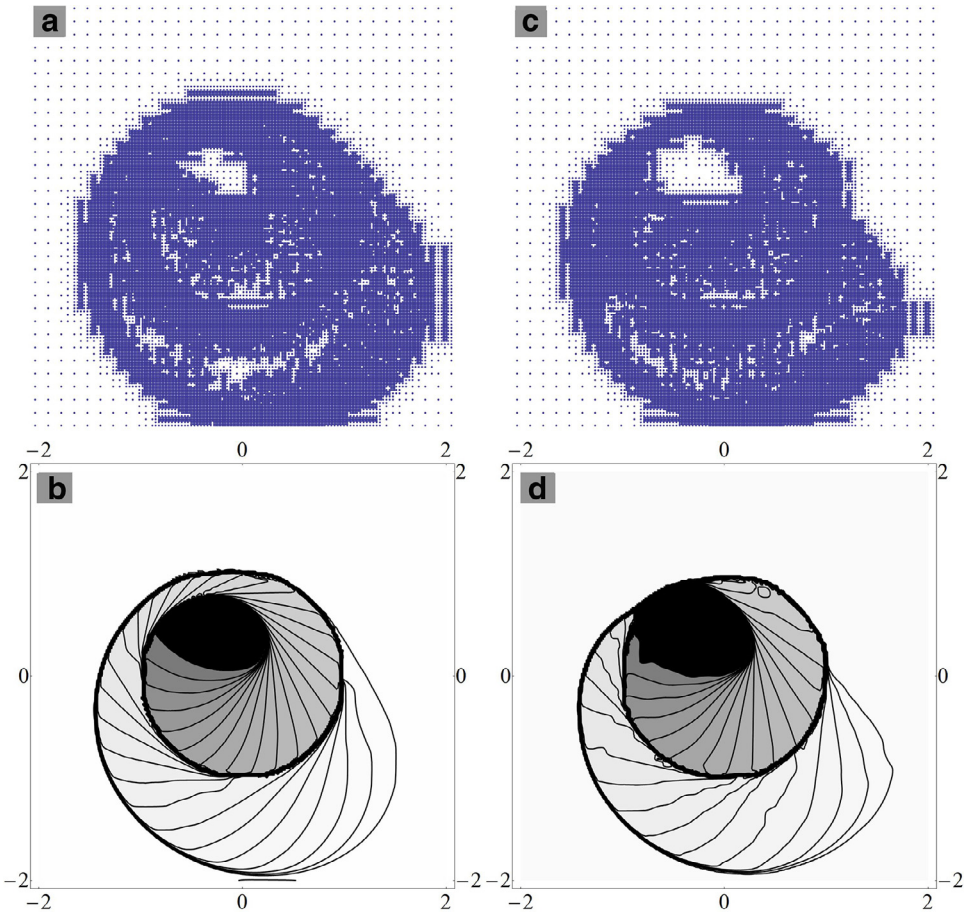

Fig. 25. Adaptive solutions of 2-D non-convex conservation law system at $t = 1$; a, b) obtained with θ-adaptive KT scheme; c, d) based on the KT scheme with $\theta = 2$.

9. Conclusion

In this study, a wavelet-based adaptation procedure is properly integrated with central/central-upwind high resolution schemes for simulation of first order hyperbolic PDEs. It is shown that central high-resolution schemes become unstable on non-uniform cells even those have gradual grid density variations. This is because, the NVSF criterion is not satisfied by central schemes. Since their slope/flux limiters do not remain TVD on irregular cell-centered cells. Two key ideas are followed to remedy the instability problem: 1) replacing local irregular grids with abrupt changing with grids having gradual variations (replacing an ill-posed problem with a nearly well-posed one); 2) studying the performance of MINMOD limiters on irregular cells. The grid modification stage is done in the framework of the multiresolution analysis. The TVD conditions are reviewed and provided for non-uniform cells. It is shown that on cell-centered cells, limiter definitions should be modified. Another approach is using of non-cell-centered cells. In this case, common MINMOD limiters can be used without modification. The TVD conditions are derived for both cell-centered and non-cell-centered cells. Based on these conditions, proper configuration of adapted cells and corresponding cell-centers are derived. It is shown that the cell-center shifting is necessary only in some cells acting as transmitting cells. They connect surrounding uniform cells with different cell lengths.

The local truncation errors for 1-D and 2-D problems are provided on non-uniform cells for convergence studying. Also the concept of the numerical entropy production is investigated for uniqueness insurance. These two concepts have also been used as criteria for grid adaptation. In this regard, performance of these concepts are compared with the wavelet-based algorithm. It is numerically shown that: 1) the numerical entropy production can not detect some phenomena such as contact discontinuities; 2) this concept also have enough values in rarefaction domains. This can lead to unnecessary concentration of grid points in such regions (this can also be seen in [40,41]); 3) it seems that the performance of the local truncation errors as detector is better than the numerical entropy production; 4) wavelets can properly detect all of the shock waves, rarefaction regions, and contact discontinuities.

Non-linear hyperbolic systems with non-convex fluxes are studied. It is shown by local truncation errors that both physical and non-physical solutions converge to weak solutions. Both method (flux/slope limiters) and grid adaptations are used for capturing physical solutions.

In conclusion, we can summarize the current study and its results as:

1. Developing TVD criteria for non-uniform non-centered cells and controlling the performance of MINMOD limiters on such cells. In this regard, central/central-upwind schemes can handle irregular cells,
2. However, these TVD criteria are for the structured multidimensional cells,
3. Proposing a proper variation of grid density (adapted ones) in the framework of the MRA. It is shown that for stable solutions, the minimum number of added points in each direction of an adapted point is: a) in the same resolution level: $N_s = 1$, b) in the successive coarser level: $N_c = 1$.
4. Generally, the MRA-based adaptation can considerably compress cell/grid numbers (around less than 15 percent) for problems with localized solutions and few numbers of discontinuities; for instance, for the Sod problem, this ratio is lower than $130/(2^{11} + 1) = 0.064$ for the KT scheme and is lower than $220/(2^{11} + 1) = 0.107$ for the $M2$ scheme,
5. A proper selection of threshold values (ϵ) may need the trial error method; however, for normalized solution values, the range $\epsilon \in \left(10^{-5}, 10^{-4}\right)$ can be recommended,

6. Updating the estimation of the local truncation errors directly on non-uniform cells,
7. Studying the performance of the numerical entropy production directly on irregular cells,
8. Studying the performance of the MINMOD limiters with adaptive dissipation (controlled by the parameterθ) for the simulation of non-convex hyperbolic PDEs.

Acknowledgments

The authors gratefully acknowledge the financial support of Iran National Science Foundation (INSF).

Appendix A. Central high-resolution schemes on non-centered non-uniform 1-D cells

By using the cell-centered non-uniform cells, the TVD stability condition does not satisfy without altering definition of slope/flux limiters. To preserve the TVD condition without limiter definition modification, it will be shown that by shifting cell centers in some cells, the TVD condition can be reached. These cells act as transmitting cells connecting two surrounding uniform cells of different lengths. By such cell-center shifting, a new source of the truncation error will be introduced. Effects of this new error will be discussed.

Considering the REP, the full-discrete and semi-discrete forms of the scalar hyperbolic equation $u_t + F(u)_x = 0$ will be provided on non-centered non-uniform cells. For generality, it is assumed that cell centers x_j are not located at cell centers (viz: $x_j \neq (x_{j-1/2} + x_{j+1/2})/2$); so, the left and right cell edge positions are: $x_{j-1/2} := x_j - (1-p_j)\Delta x_j$ and $x_{j+1/2} := x_j + p_j \Delta x_j$, where $0 < p_j < 1$ (for $p_j = 1/2$ the cell center x_j is the middle point of jth cell).

A-1. The reconstruction and evolution stages

1. The spatio-temporal volume $\Delta x_{j+1/2} \times \Delta t$ is considered, where $\Delta x_{j+1/2} := x^n_{j+1/2,r} - x^n_{j+1/2,l} = 2\Delta t a^n_{j+1/2}$, and $\Delta t := t^{n+1} - t^n$. By averaging on this volume and considering the midpoint integration rule in time, the solution $w^{n+1}_{j+1/2} := w(x_{j+1/2}, t^n)$ can be obtained as:

$$\begin{aligned} w^{n+1}_{j+1/2} &= \frac{1}{\Delta x_{j+1/2}} \int_{x^n_{j+1/2,l}}^{x^n_{j+1/2,r}} u(x, t^{n+1})\,\mathrm{d}x \\ &= \frac{1}{\Delta x_{j+1/2}} \int_{x^n_{j+1/2,l}}^{x^{n}_{j+1/2,r}} u(x, t^{n})\,\mathrm{d}x \\ &\quad - \frac{1}{\Delta x_{j+1/2}} \int_{t^n}^{t^{n+1}} \Big[F(u^n_{j+1/2,r}) - F(u^n_{j+1/2,l})\Big]\,\mathrm{d}t \\ &= \frac{1}{4}\Bigg(- \Delta t a^n_{j+\frac{1}{2}} \big(u_x\big)^n_j + \Delta t a^n_{j+\frac{1}{2}} \big(u_x\big)^n_{j+1} + 2\Delta x_j p_j \big(u_x\big)^n_j \\ &\quad + 2\Delta x_{j+1}\big(p_{j+1} - 1\big)\big(u_x\big)^n_{j+1} + 2u_j + 2u_{j+1}\Bigg) \\ &\quad - \frac{1}{2a^n_{j+\frac{1}{2}}}\left(F^{n+\frac{1}{2}}_{j+\frac{1}{2},r} - F^{n+\frac{1}{2}}_{j+\frac{1}{2},l}\right), \end{aligned} \tag{A-1}$$

where $F^{n+\frac{1}{2}}_{j+\frac{1}{2},r} := F(u(x_{j+\frac{1}{2},r}, t^{n+\frac{1}{2}}))$ and $F^{n+\frac{1}{2}}_{j+\frac{1}{2},l} := F(u(x_{j+\frac{1}{2},l}, t^{n+\frac{1}{2}}))$.

2. The spatio-temporal volume $\Delta x^{l-r}_j \times \Delta t$ is considered, where $\Delta x^{l-r}_j := x^n_{j+1/2,l} - x^n_{j-1/2,r} = \Delta x_j - \Delta t(a^n_{j-1/2} + a^n_{j+1/2})$. By averaging on this volume and considering the midpoint rule in time, evolved solution $w^{n+1}_j := w(x_j, t^{n+1})$ is:

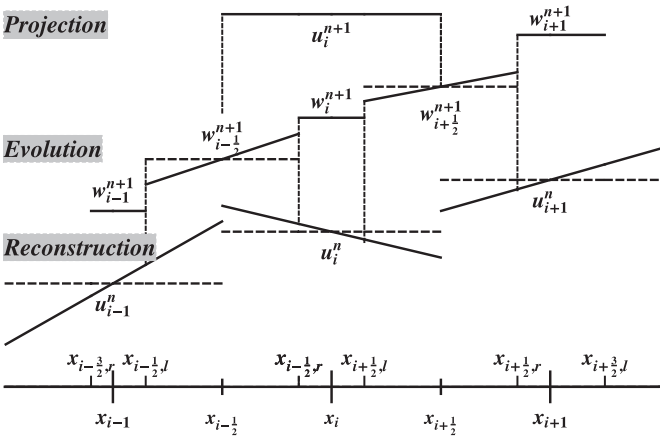

Fig. A.1. The reconstruction/evolution/projection concept to have a second order accuracy in the spatial domain.

$$\begin{aligned} w^{n+1}_j &= \frac{1}{\Delta x^{l-r}_j} \int_{x^n_{j-1/2,r}}^{x^n_{j+1/2,l}} u(x, t^{n+1})\,\mathrm{d}x \\ &= \frac{1}{\Delta x^{l-r}_j} \int_{x^n_{j-1/2,r}}^{x^n_{j+1/2,l}} u(x, t^{n})\,\mathrm{d}x \\ &\quad - \frac{1}{\Delta x^{l-r}_j} \int_{t^n}^{t^{n+1}} \Big[F(u^n_{j+1/2,l}) - F(u^n_{j-1/2,r})\Big]\,\mathrm{d}t \\ &= \frac{1}{2}\left(\Delta t\left(a^n_{j-\frac{1}{2}} - a^n_{j+\frac{1}{2}}\right)\big(u_x\big)^n_j + \Delta x_j\big(2p_j - 1\big)\big(u_x\big)^n_j + 2u_j\right) \\ &\quad - \frac{\Delta t\left(F^{n+\frac{1}{2}}_{j+\frac{1}{2},l} - F^{n+\frac{1}{2}}_{j-\frac{1}{2},r}\right)}{\Delta x_j - \Delta t\left(a^n_{j-\frac{1}{2}} + a^n_{j+\frac{1}{2}}\right)}. \end{aligned} \tag{A-2}$$

3. Regarding volume $\Delta x_{j-1/2} \times \Delta t$, where $\Delta x_{j-1/2} := x^n_{j-1/2,l} - x^n_{j-1/2,r}$, evolved solution $w^{n+1}_{j-1/2} := w(x_{j-1/2}, t^{n+1})$ can be obtained with the similar procedure explained in (A.1).

Considering $w^{n+1}_{j+1/2}$, w^{n+1}_j, and $w^{n+1}_{j-1/2}$ definitions in Eqs. (A.1) and (A.2), a piecewise-linear approximation on the staggered grid in the evolution stage is (see Fig. A.1):

$$\begin{aligned} &\tilde{w}(x, t^{n+1}) \\ &:= \sum_j \left\{ w^{n+1}_{j+1/2} + (u_x)^{n+1}_{j+1/2}\big(x - x_{j+1/2}\big)\mathbf{1}_{\left[x^n_{j+1/2,l}, x^n_{j+1/2,r}\right]} + w^{n+1}_j \mathbf{1}_{\left[x^n_{j-1/2,r}, x^n_{j+1/2,l}\right]} \right\}, \end{aligned}$$

where $(u_x)^{n+1}_{j\pm 1/2}$ denote limited derivatives and $\mathbf{1}_{[a,b]}$ shows a unit function on spatial interval $[a, b]$.

A-2. The projection stage

The fully discrete second-order central scheme can be obtained by averaging $\tilde{w}(x, t^{n+1})$ on interval $\left[x_{j-1/2}, x_{j+1/2}\right]$, as:

$$\begin{aligned} \bar{u}^{n+1}_j &= \frac{1}{\Delta x_j} \int_{x_{j-1/2}}^{x_{j+1/2}} \tilde{w}(x, t^{n+1})\,\mathrm{d}x \\ &= \frac{1}{4\Delta x_j}\Bigg[2\Bigg(\Delta t\left(F^{n+\frac{1}{2}}_{j-\frac{1}{2},l} - F^{n+\frac{1}{2}}_{j+\frac{1}{2},l} + F^{n+\frac{1}{2}}_{j-\frac{1}{2},r} - F^{n+\frac{1}{2}}_{j+\frac{1}{2},r}\right) \\ &\quad + \Delta x_j\left(\Delta x_j\big(2p_j - 1\big)\big(u_x\big)^n_j + 2u_j\right)\Bigg) \\ &\quad + 2\Delta t a^n_{j-\frac{1}{2}}\left(\Delta x_{j-1} p_{j-1}\big(u_x\big)^n_{j-1} - \Delta x_j\big(p_j - 1\big)\big(u_x\big)^n_j + u_{j-1} - u_j\right) \end{aligned}$$

$$+2\Delta t a^n_{j+\frac{1}{2}}\left(\Delta x_j(-p_j)(u_x)^n_j+\Delta x_{j+1}(p_{j+1}-1)(u_x)^n_{j+1}-u_j+u_{j+1}\right)$$
$$-\Delta t^2\left(a^n_{j-\frac{1}{2}}\right)^2\left((u_x)^n_{j-1}+(u_x)^n_j-2(u_x)^{n+1}_{j-1/2}\right)$$
$$+\Delta t^2\left(a^n_{j+\frac{1}{2}}\right)^2\left((u_x)^n_j+(u_x)^n_{j+1}-2(u_x)^{n+1}_{j+1/2}\right)\Bigg], \quad (A\text{-}3)$$

where $\bar{u}^{n+1}_j$ denotes the average of solution $u(x,t^{n+1})$ on the cell $I_j\in[x_{j-1/2},x_{j+1/2}]$.

A-3. The semi-discrete form

Regarding the full discrete form (A.3), for small enough Δt values, the following approximations can be assumed: 1) ignoring of terms corresponding to Δt^2; 2) $F^{n+\frac{1}{2}}_{j\pm\frac{1}{2},r}\approx F^n_{j\pm\frac{1}{2},r}=F^R_{j\pm1/2}$ and $F^{n+\frac{1}{2}}_{j\pm\frac{1}{2},l}\approx F^n_{j\pm\frac{1}{2},l}=F^L_{j\pm1/2}$ (due to the Taylor expansion in smooth zones). By these approximations, Eq. (A.3) can be rearranged and rewritten as:

$$\frac{\bar{u}^{n+1}_j-u^n_j}{\Delta t}=\approx\frac{1}{4\Delta x_j}\Bigg\{2\left(-F^n_{j+\frac{1}{2},l}-F^n_{j+\frac{1}{2},r}+F^n_{j-\frac{1}{2},l}+F^n_{j-\frac{1}{2},r}\right)$$
$$-2\left(-u_{j-1}a^n_{j-\frac{1}{2}}+u_ja^n_{j-\frac{1}{2}}+u_ja^n_{j+\frac{1}{2}}-u_{j+1}a^n_{j+\frac{1}{2}}\right)$$
$$+2\left(\Delta x_{j-1}p_{j-1}a^n_{j-\frac{1}{2}}(u_x)^n_{j-1}+\Delta x_j\left(a^n_{j-\frac{1}{2}}-p_j\left(a^n_{j-\frac{1}{2}}+a^n_{j+\frac{1}{2}}\right)\right)(u_x)^n_j\right)$$
$$+2\left(\Delta x_{j+1}(p_{j+1}-1)a^n_{j+\frac{1}{2}}(u_x)^n_{j+1}\right)\Bigg\}-\left(\frac{1}{2}-p_j\right)(u_x)^n_j\frac{\Delta x_j}{\Delta t}. \quad (A\text{-}4)$$

Since $u^L_{j+1/2}:=u_j+p_j\Delta x_j(u_x)^n_j$ and $u^R_{j-1/2}:=u_j-(1-p_j)\Delta x_j(u_x)^n_j$, (A.4) can be rewritten as:

$$\frac{\bar{u}^{n+1}_j-u^n_j}{\Delta t}+\frac{F^*_{j+1/2}-F^*_{j-1/2}}{\Delta x_j}\approx Q^n_j, \quad (A\text{-}5)$$

where $Q^n_j:=-\left(\frac{1}{2}-p_j\right)(u_x)^n_j\frac{\Delta x_j}{\Delta t}$. On the other hand, spatial distance between the midpoint $\bar{x}_j$ and x_j is: $\delta_j:=x_j-\bar{x}_j=\left[x_{j+1/2}-p_j\Delta x_j\right]-\left[x_{j+1/2}-\frac{\Delta x_j}{2}\right]=(\frac{1}{2}-p_j)\Delta x_j$. So average solutions $\bar{u}^n_j$ relate to point value solutions, u^n_j as: $u^n_j\approx\bar{u}^n_j+\delta_j\times(u_x)^n_j$. In this regard, Eq. (A.5) can be written as:

$$\frac{\bar{u}^{n+1}_j-\bar{u}^n_j}{\Delta t}+\frac{F^*_{j+1/2}-F^*_{j-1/2}}{\Delta x_j}\approx 0. \quad (A\text{-}6)$$

So, at the limit $\Delta t\to 0$, this equation becomes:

$$\frac{d\bar{u}_j}{dt}+\frac{F^*_{j+1/2}-F^*_{j-1/2}}{\Delta x_j}=0. \quad (A\text{-}7)$$

So, in the sense of average solutions, the semi-discrete form remains conservative. We can rewrite Eq. (A.5) based on point value solutions, u^n_j; for this purpose, we approximate u^{n+1}_j as $u^{n+1}_j=\bar{u}^{n+1}_j+\delta_j\times(u_x)^{n+1}_j$; so we have:

$$\frac{u^{n+1}_j-u^n_j}{\Delta t}+\frac{F^*_{j+1/2}-F^*_{j-1/2}}{\Delta x_j}\approx Q^n_j-Q^{n+1}_j, \quad (A\text{-}8)$$

We conclude this section with the following remarks regarding (A.5).

1. The term Q acts as a new source of the truncation error,
2. Effects of Δt in Q can be controlled by small-enough spatial sampling steps Δx_j. This can be done by a proper grid adaptation procedure around high-gradient zones,
3. If x_j is in the middle of the jth cell, i.e. $p=1/2$, the truncation error Q vanishes: $Q=0$,
4. Around discontinuities, since limited slopes $(u_x)^n_j$ are nearly zero, the error Q approaches to zero,
5. Average solution on jth cell is $(u^n_j)_{ave}=u^n_j+Q\times\Delta t$.

References

[1] Sweldens W, Schröder P. Building your own wavelets at home. In: Wavelets in the Geosciences. Springer; 2000. p. 72–107.
[2] Griebel M, Koster F. Adaptive wavelet solvers for the unsteady incompressible navier-stokes equations. In: Málek J, Nečas J, Rokyta M, editors. Advances in Mathematical Fluid Mechanics. Springer Berlin Heidelberg; 2000. p. 67–118. ISBN 978-3-540-67786-4.
[3] Yousefi H, Noorzad A, Farjoodi J. Simulating 2D waves propagation in elastic solid media using wavelet based adaptive method. J Sci Comput 2010;42(3):404–25.
[4] Bürger R, Kozakevicius A. Adaptive multiresolution WENO schemes for multi-species kinematic flow models. J Comput Phys 2007;224(2):1190–222.
[5] Cohen A, Kaber S, Müller S, Postel M. Fully adaptive multiresolution finite volume schemes for conservation laws. Math Comp 2003;72(241):183–225.
[6] Müller S. Adaptive multiscale schemes for conservation laws, 27. Springer; 2003.
[7] Dahmen W, Gottschlich-Müller B, Müller S. Multiresolution schemes for conservation laws. Numer Math 2001;88(3):399–443.
[8] Harten A. Multiresolution algorithms for the numerical solution of hyperbolic conservation laws. Comm Pure Appl Math 1995;48(12):1305–42.
[9] Domingues MO, Gomes SM, Roussel O, Schneider K. An adaptive multiresolution scheme with local time stepping for evolutionary PDEs. J Comput Phys 2008;227(8):3758–80.
[10] Alves MA, Cruz P, Mendes A, Magalhães FD, Pinho FT, Oliveira PJ. Adaptive multiresolution approach for solution of hyperbolic PDEs. Comput Methods Appl Mech Eng 2002;191(36):3909–28.
[11] Yousefi H, Noorzad A, Farjoodi J, Vahidi M. Multiresolution-based adaptive simulation of wave equation. AMIS 2012;6(1S):47S–58S.
[12] Yousefi H, Noorzad A, Farjoodi J. Multiresolution based adaptive schemes for second order hyperbolic PDEs in elastodynamic problems. Appl Math Modell 2013;37(12):7095–127.
[13] Cruz P, Mendes A, Magalhães FD. Using wavelets for solving PDEs: an adaptive collocation method. Chem Eng Sci 2001;56(10):3305–9.
[14] Cruz P, Mendes A, Magalhães FD. Wavelet-based adaptive grid method for the resolution of nonlinear PDEs. AIChE J 2002;48(4):774–85.
[15] Jameson L, Miyama T. Wavelet analysis and ocean modeling: A dynamically adaptive numerical method "WOFD-AHO". Mon Wea Rev 2000;128(5):1536–49.
[16] Butcher JC. Numerical methods for ordinary differential equations. John Wiley & Sons; 2008.
[17] Ascher UM. Numerical methods for evolutionary differential equations, 5. Siam; 2008.
[18] Cebeci T. Computational fluid dynamics for engineers: from panel to Navier-Stokes methods with computer programs. Springer; 2005.
[19] Gottlieb D, Hesthaven JS. Spectral methods for hyperbolic problems. J Comput Appl Math 2001;128(1):83–131.
[20] Bertoluzza S, Castro LM. Adaptive wavelet collocation for elasticity: first results. Pavia, Italy: IAN–CNR; 2001.
[21] Vasilyev OV, Kevlahan NK-R. An adaptive multilevel wavelet collocation method for elliptic problems. J Comput Phys 2005;206(2):412–31.
[22] Alam JM, Kevlahan NK-R, Vasilyev OV. Simultaneous space-time adaptive wavelet solution of nonlinear parabolic differential equations. J Comput Phys 2006;214(2):829–57.
[23] Mehra M, Kevlahan NK-R. An adaptive wavelet collocation method for the solution of partial differential equations on the sphere. J Comput Phys 2008;227(11):5610–32.
[24] Yousefi H, Taghavi Kani A, Mahmoudzadeh Kani I. Response of a spherical cavity in a fully-coupled thermo-poro-elastodynamic medium by cell-adaptive second-order central high resolution schemes. Underground Space 2018;3(3):206–17.
[25] Darwish MS, Moukalled FH. Normalized variable and space formulation methodology for high-resolution schemes. Numer Heat Transfer, Part B 1994;26(1):79–96.
[26] Santos JC, Cruz P, Alves MA, Oliveira PJ, Magalhães FD, Mendes A. Adaptive multiresolution approach for two-dimensional PDEs. Comput Methods Appl Mech Eng 2004;193(3–5):405–25.
[27] Kurganov A, Tadmor E. New high-resolution central schemes for nonlinear conservation laws and convection–diffusion equations. J Comput Phys 2000;160(1):241–82.
[28] Kurganov A, Petrova G. Central schemes and contact discontinuities. ESAIM: M2AN 2000;34(06):1259–75.
[29] Kurganov A, Lin C-T. On the reduction of numerical dissipation in central-upwind schemes. Commun Comput Phys 2007;2(1):141–63.
[30] Nessyahu H, Tadmor E. Non-oscillatory central differencing for hyperbolic conservation laws. J Comput Phys 1990;87(2):408–63.
[31] Berger M, Aftosmis MJ, Murman SM. Analysis of slope limiters on irregular grids. AIAA Pap 2005;490:2005.
[32] Zeng X. A general approach to enhance slope limiters on non-uniform grids. CoRR 2013:1–35.
[33] Karni S, Kurganov A, Petrova G. A smoothness indicator for adaptive algorithms for hyperbolic systems. J Comput Phys 2002;178(2):323–41.
[34] Karni S, Kurganov A. Local error analysis for approximate solutions of hyperbolic conservation laws. Adv Comput Math 2005;22(1):79–99.
[35] Tadmor E. Local error estimates for discontinuous solutions of nonlinear hyperbolic equations. SIAM J Numer Anal 1991;28(4):891–906.
[36] Tadmor E, Tang T. Pointwise error estimates for scalar conservation laws with piecewise smooth solutions. SIAM J Numer Anal 1999;36(6):1739–58.
[37] Puppo G. Numerical entropy production on shocks and smooth transitions. J Sci Comput 2002;17(1–4):263–71.
[38] Puppo G. Numerical entropy production for central schemes. SIAM J Sci Comput 2004;25(4):1382–415.

[39] Kurganov A, Petrova G, Popov B. Adaptive semidiscrete central-upwind schemes for nonconvex hyperbolic conservation laws. SIAM J Sci Comput 2007;29(6):2381–401.
[40] Puppo G, Semplice M. Numerical entropy and adaptivity for finite volume schemes.. Commun Comput Phys 2011;10(5):1132.
[41] Ersoy M, Golay F, Yushchenko L. Adaptive multiscale scheme based on numerical density of entropy production for conservation laws. Cent Eur J Math 2013;11(8):1392–415.
[42] Mallat S. A wavelet tour of signal processing. Academic press; 1999.
[43] LeVeque RJ, Le Veque RJ. Numerical methods for conservation laws, 132. Springer; 1992.
[44] Trangenstein JA. Numerical solution of hyperbolic partial differential equations. Cambridge University Press; 2009.
[45] Yousefi H, Mohammadi S, Rabczuk T. Multiscale polynomial-based high-order central high resolution schemes. J Sci Comput 2019. Accepted.
[46] Yousefi H, Kani AT, Kani IM. Multiscale RBF-based central high resolution schemes for simulation of generalized thermoelasticity problems. Front Struct Civil Eng 2018:1–27.
[47] Li BQ. Discontinuous finite elements in fluid dynamics and heat transfer. Springer Science & Business Media; 2006.
[48] Yoon Y-C, Schaefferkoetter P, Rabczuk T, Song J-H. New strong formulation for material nonlinear problems based on the particle difference method. Eng Anal Bound Elem 2019;98:310–27.
[49] Yoon Y-C, Song J-H. Extended particle difference method for moving boundary problems. Comput Mech 2014a;54(3):723–43.
[50] Yoon Y-C, Song J-H. Extended particle difference method for weak and strong discontinuity problems: part ii. formulations and applications for various interfacial singularity problems. Comput Mech 2014b;53(6):1105–28.
[51] Yoon Y-C, Song J-H. Extended particle difference method for weak and strong discontinuity problems: part i. derivation of the extended particle derivative approximation for the representation of weak and strong discontinuities. Comput Mech 2014c;53(6):1087–103.
[52] Kuzmin D. On the design of general-purpose flux limiters for finite element schemes. I. scalar convection. J Comput Phys 2006;219(2):513–31.
[53] Kuzmin D, Turek S. High-resolution FEM-TVD schemes based on a fully multidimensional flux limiter. J Comput Phys 2004;198(1):131–58.
[54] Donoho DL. Interpolating wavelet transforms. Department of Statistics, Stanford University 1992;2(3).
[55] Guermond J-L, Pasquetti R, Popov B. Entropy viscosity method for nonlinear conservation laws. J Comput Phys 2011;230(11):4248–67.
[56] Harten A. High resolution schemes for hyperbolic conservation laws. J Comput Phys 1983;49(3):357–93.
[57] Jameson A, Lax PD. Conditions for the construction of multi-point total variation diminishing difference schemes. Appl Numer Math 1986;2(3):335–45.
[58] Osher S. Riemann solvers, the entropy condition, and difference. SIAM J Numer Anal 1984;21(2):217–35.
[59] Sanders R. On convergence of monotone finite difference schemes with variable spatial differencing. Math Comp 1983;40(161):91–106.
[60] Tadmor E. Convenient total variation diminishing conditions for nonlinear difference schemes. SIAM J Numer Anal 1988;25(5):1002–14.
[61] Osher S. Convergence of generalized MUSCL schemes. SIAM J Numer Anal 1985;22(5):947–61.
[62] Jain S, Tsiotras P, Zhou H-M. A hierarchical multiresolution adaptive mesh refinement for the solution of evolution PDEs. SIAM J Sci Comput 2008;31(2):1221–48.
[63] Shu C-W, Osher S. Efficient implementation of essentially non-oscillatory shock–capturing schemes, II. In: Upwind and High-Resolution Schemes. Springer; 1989. p. 328–74.
[64] Holmström M. Solving hyperbolic PDEs using interpolating wavelets. SIAM J Sci Comput 1999;21(2):405–20.
[65] Sod GA. A survey of several finite difference methods for systems of nonlinear hyperbolic conservation laws. J Comput Phys 1978;27(1):1–31.
[66] Lax PD. Weak solutions of nonlinear hyperbolic equations and their numerical computation. Comm Pure Appl Math 1954;7(1):159–93.
[67] Shu C-W, Osher S. Efficient implementation of essentially non-oscillatory shock-capturing schemes. J Comput Phys 1988;77(2):439–71.
[68] Lie K-A, Noelle S. On the artificial compression method for second-order nonoscillatory central difference schemes for systems of conservation laws. SIAM J Sci Comput 2003;24(4):1157–74.
[69] Toro EF, Toro EF. Riemann solvers and numerical methods for fluid dynamics, 16. Springer; 1999.